

Kapteyn Astronomical Institute

A Mid-Infrared Spectral Atlas of Simple Organic
Chemistry in the Protoplanetary Disk of
FT Tauri

August 22, 2016

Author: N.O. Oberg
Supervisor: Dr. I.E.E Kamp
Co-Supervisor: dr. S.Antonellini



university of
 groningen

faculty of mathematics
and natural sciences

Abstract

Context: The Mid-InfraRed Instrument (MIRI) will fly on the James Webb Space Telescope (JWST) nominally in late 2018. MIRI contains a spectrograph of spectral resolution ~ 3000 in the band 5-28 μm . One of the uses of MIRI will be the study of protoplanetary disks (PPDs).

Aims: Assess the detectability of organic molecular features in various simulated PPDs and the typical exposure times needed. Determine if different types of disks produce different organic spectra. These results will help plan the MIRI guaranteed observing time.

Methods: I have compiled a library of mid-infrared emission spectra using the ProDiMo (PROtoplanetary DIsc MOdel) software package. I used a fast line radiative transfer code FLiTs to compute spectra based on the ProDiMo output. A mid-infrared spectrum of FT Tau made by the *Spitzer* space telescope was used for analysis of the resulting spectra. Afterwards I apply sensitivity estimates for the JWST/MIRI MRS with the resulting spectra to determine the minimum exposure time required to guarantee the detection of various spectral lines of interest.

Acknowledgments

I would like to thank my supervisor Dr. Inga Kamp for her guidance, her clear and well reasoned explanations, the interesting conversations that we held, and her ability to rapidly diagnose my mistakes. I would also like to thank dr. Stefano Antonellini for his enthusiastic support and deep understanding of the subject which he shared with me. Furthermore, I wish to thank the rest of the staff of the Kapteyn Astronomical Institute and the Rijksuniversiteit Groningen for equipping me with the understanding, patience, and technical skill necessary to complete this thesis, as well as my friends for encouraging and tolerating me. Finally, I would like to thank my parents who supported me unequivocally throughout the entire ordeal.

Contents

1	Introduction	5
1.1	Protoplanetary Disk Observation	6
1.2	Disk Formation	8
1.3	Disk Properties	9
1.3.1	Disk Mass	9
1.3.2	Disk Size	10
1.3.3	Vertical and Radial Structure	10
1.3.4	Content and Chemistry	11
1.4	Emission Lines in Disks	12
1.4.1	Emission Mechanisms and Energy Levels	12
1.4.2	Gas Emission	13
1.4.3	Dust Emission	14
1.4.4	The MIR Organic Spectrum	14
1.5	Stars with Disks	14
1.5.1	FT Tauri in Taurus-Auriga	15
1.6	MIRI	15
1.7	Significance	16
2	Modeling Disks	17
2.1	ProDiMo	17
2.2	ProDiMo Disk Structure	17
2.3	ProDiMo Continuum Radiative Transfer	18
2.3.1	Stellar Irradiation	18
2.4	ProDiMo Chemistry	19
2.5	ProDiMo Gas Thermal Balance; Heating and Cooling	19
2.5.1	Heating Processes	19
2.5.2	Cooling Processes	20
2.6	The Fast Line Tracing System	21
2.7	Noise and Spectral Resolving Power Simulation	22
2.8	MIRI sensitivity estimation	22
2.8.1	FT Tau as parametrized in ProDiMo	23
3	Results	24
3.1	Comparing ProDiMo+FLiTs and Spitzer	24
3.1.1	ProDiMo M_{gas} parameter exploration	27
3.1.2	ProDiMo PAH abundance parameter exploration	29
3.1.3	ProDiMo chemical heating efficiency parameter exploration	30
3.1.4	ProDiMo H_2 cosmic ray ionization parameter exploration	31
3.1.5	ProDiMo stellar parameter exploration	32
3.2	The Spectral Atlas	32
3.3	Exposure Time Results	33
4	Discussion	33
4.1	Contrasting ProDiMo+FLiTs and Spitzer	33
4.1.1	Continuum Flux ProDiMo+FLiTs vs. Spitzer FT Tau	34
4.2	M_{gas} and Impossible Disks	35
4.3	Other ProDiMo Parameter Explorations	36
5	Conclusion	38
	References	39
	Appendices	46

1 Introduction

Carbonaceous chondrites are meteorites that are believed to have accreted directly from protoplanetary disk (PPD) material during the birth of the solar system. They have been found to contain a wide variety of organic compounds including carboxylic acids, CO₂, aliphatic and aromatic hydrocarbons, amino acids, alcohols, ketones, aldehydes, amines, amides, sulfonic acids, phosphonic acids, and pyrimidines such as Uracil and Thymine (nucleobases in RNA and DNA respectively) [Sephton, 2002].

An isotopic ratio dating analysis of Ca-Al-rich inclusions found in the carbonaceous chondrite NWA 2364 indicates that the first solid materials condensed from the Sun's protoplanetary disk 4568.22±0.17 Myr ago [Bouvier and Wadhwa, 2010], marking the approximate time of the solar system's creation. The formation of our own planetary system is thus far removed from us in time, while new systems currently in the process of formation are far removed in space. The study of this process is hence two-pronged; geological and astronomical, the latter approach being the subject of this thesis.

Cosmogeny and The Nebular Hypothesis

Cosmogenic theories of classical antiquity were the first to include naturalistic explanations for the creation of the solar system. The pre-Socratic atomist Democritus believed the Earth to have condensed from the aggregation of colliding particles, where previously there had existed only a formless void of atoms in a state of chaos. [Barnes, 2001].

Twenty centuries passed before the nascent modern speculation of philosopher-mathematician René Descartes and scientist-mystic Emanuel Swedenborg suggested a cloud or vortex-like origin for the Sun and planets. In 1755 Immanuel Kant used the principles of the newly published theory of Newtonian gravitation to qualitatively formulate a collapsing cloud theory which simultaneously explained the creation of both the Sun and planets, their confinement to the plane of the ecliptic, their aligned rotational axis and common prograde motion [Whitrow, 1967]. Later a more detailed nebular hypothesis was developed independently in the 1796 publication *Exposition du systeme du monde* by Pierre-Simon Laplace [Montgomery et al., 2009].

Laplace considered a nebula of heated gas which had been drawn into a sphere by the force of gravity and rotated slowly. Gravitational contraction of the gas cloud, initially much larger than the orbit of Neptune, would continue until the centrifugal force at some radius would equal the gravitational attraction of the central mass of the cloud. At this point a ring of material would detach from the cloud and collapse would continue further. The process would repeat until rings of material formed at several intervals around the Sun, and then later coalesced into the planets [Aitken, 1906].

Despite roughly a century of modification and general acceptance the theory was called into question as being unable to explain, among other phenomena, the distribution of angular momentum within the solar system; a paradoxical situation where the Sun, despite having 99.86% of the solar system's mass contains only 0.3% of its angular momentum [Woolfson, 1993]. Alternative and even fringe theories flourished during this period. In at least one instance the popular conscious was permeated, such that the American Association for the

Advancement of Science moved to address the widely disseminated and controversial theories presented in Immanuel Velikovsky's 1950 publication *Worlds in Collision* by creating a collection of scientific criticisms in *Scientists Confront Velikovsky* [Sagan, 1979].

Theories based on the Laplacian premise returned to general acceptance when new mechanisms to explain angular momentum transfer and other considerations were introduced by [Hoyle, 1960], [Safronov, 1972], [Lynden-Bell and Pringle, 1974], and [Prentice, 1978] and it is the cloud collapse model that forms the basis of modern research. By coupling star and planet formation to a common event, the modern theory implies that planets are a universally common phenomena that result from stellar birth. Earlier speculation that planet formation was limited to a serendipitous incident [Woolfson, 1993] in the Sun's early history was refuted by the discovery of ~ 3000 confirmed extrasolar planets and ~ 4000 extrasolar planet candidates as of 2016 [Morton et al., 2016], as well as by the direct detection and characterization of PPDs associated with large molecular clouds and star forming regions [O'dell et al., 1993]. From these detections we can infer the ubiquity of planets throughout the cosmos [Petigura et al., 2013].

1.1 Protoplanetary Disk Observation

Background on Infrared Astronomy

Absorption by H_2O , CO_2 , CH_4 , N_2O , and O_3 render the Earth's atmosphere opaque to much of the infrared (IR) radiation band with the exception of the sub/mm ($>450\mu\text{m}$) which can be observed from high-altitude arid locations. Additionally the significant Earth thermal emission background ($T=288\text{K}$) makes the $\sim 5 - 25\mu\text{m}$ range impossible to observe from the ground.

The development of space launch technology in the 1950-60's enabled the first astronomical instruments to be moved beyond the atmosphere, opening previously unobserved regions of the electromagnetic spectrum to scrutiny [Walker, 2000]. Space-based telescopes with detectors sensitive to IR radiation were constructed to study matter not visible in optical wavelengths, and which emitted thermal radiation from much cooler sources than had been previously detectable [Draine, 2011].

Matter Around Other Stars

Main Sequence (MS) stars are near-blackbody radiators, and their emission is expected to closely obey Planck's law, with the exception of absorption and emission features based on spectral classification [LeBlanc, 2010]. If a star were to be enveloped by μm sized dust grains, the matter would absorb stellar radiation and re-emit it as thermal radiation at IR wavelengths. An IR excess over a predicted stellar spectrum would imply that a star could be associated with nearby dust grains [Evans, 1993] as in Figure 1.

The initial detection of cool ($T=100\text{-}500\text{K}$) matter surrounding other stars was made by the Infrared Astronomical Satellite (IRAS) which discovered an IR excess from several young stars such as the nearby zero-age main sequence (ZAMS) star β Pictoris [Helou and Walker, 1988] but also the MS A0 star α Lyrae was shown to have an excess of radiation in the mid- to far- infrared

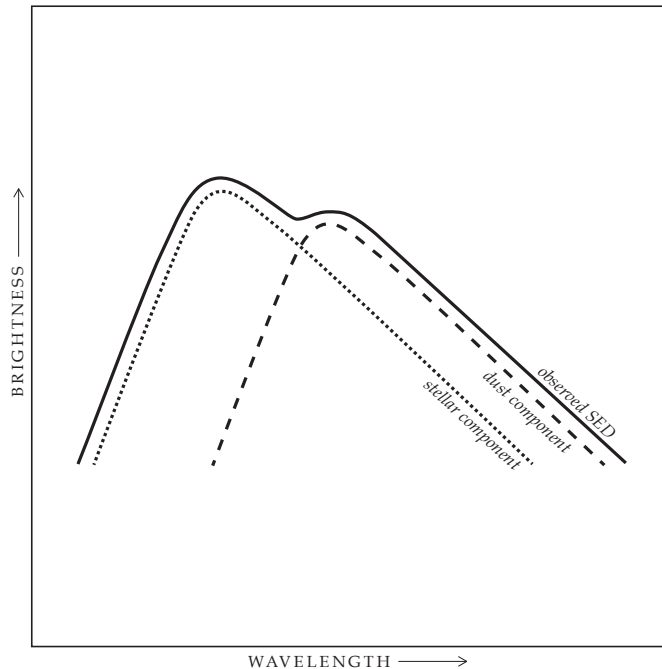


Figure 1: Schematic representation of the infrared excess caused by circumstellar dust (image credit Silke Ceulemans)

extending approximately 85AU from the star [Aumann et al., 1984, Gray, 2007] and others. These observations were interpreted as small solid particles in orbit around the stars having condensed from a protostellar nebula rather than having been expelled from the stars [Aumann et al., 1984].

Measurement of the CO ($J = 1 \rightarrow 0$) emission by the three-element millimeter wave interferometer at the Owens Valley observatory showed the emitting matter to be in flattened rotating structures [Beckwith et al., 1986]. Confirmation of the protoplanetary nature of the disks was made by optical HST observations showing protoplanetary disks silhouetted against the star-forming Orion nebula [O’de11 et al., 1993, Ricci et al., 2008].

Higher spectral resolution ($R = 600$) surveys of disks by the *Spitzer* space telescope and radio surveys in the mid-2000s revealed the presence of various simple molecules such as H_2 , CO_2 , H_2O and HCN in disks [Carr and Najita, 2008, Thi et al., 2004, van Zadelhoff et al., 2001] but also more complex volatiles and refractory silicate grains. Currently the structure of rings in disks such as HL Tauri is being probed by sub-mm long baseline interferometric observatories such as ALMA [ALMA Partnership et al., 2015], with an angular resolution of at 0.87mm of $0.025''$, a 240-fold improvement over the HL Tauri observations of [Beckwith et al., 1986] of $\sim 6''$. Potential protoplanets have been indirectly confirmed to be manipulating the dynamics of disk structure [Garufi et al., 2016].

It is now understood that disks are found around almost all low mass stars

shortly after their formation. For several million years these disks persist, and are eventually lost to their mass being accreted onto their star, being photo-evaporated, and being condensed into solids and planetesimals [Williams and Cieza, 2011].

1.2 Disk Formation

PPDs form during the process of star birth. Large molecular clouds in the ISM are supported by rotation, magnetic fields, and thermal gas pressure. Initially, turbulence [McKee and Ostriker, 2007] or triggering events (such as supernovae shock-fronts [Draine, 2011]) impinging on cold and dense clouds cause regions of overdensity. These regions become sufficiently dense to violate the Jeans criterion for gravitational stability

$$M_J = \left(\frac{\pi}{6}\right) \frac{c_s^3}{G^{3/2}\rho^{1/2}} \quad (1)$$

with M_J the cloud mass, c_s the speed of sound in the cloud, G the gravitational constant and ρ the density [Jeans, 1902]. The cloud starts to fragment as matter falls towards the nearest gravitationally unstable overdensities. It collapses until individual fragments of diameter $\sim 10^4$ AU achieve hydrostatic equilibrium as warm spheres of gas and dust that continue to accrete matter from a surrounding envelope [Scilla, 2016].

The role of magnetic fields during this stage is uncertain [Williams and Cieza, 2011]. Polarimetric studies show concentrated magnetic field lines at the center of these spheres [Girart et al., 2006] but the magnetic field strength should be insufficient to support the central cores against their own gravity [Crutcher et al., 2009]. Deuterium-Lithium fusion begins in the cores at a critical temperature and density and the spherical masses becomes protostars which are still surrounded entirely by the nebulous envelope. The envelope surrounding the protostar, initially spherical, flattens into a disk as angular momentum is conserved during in-fall. This disk extends outward to the centrifugal radius

$$R(t) \propto \Omega^2 t^3 \quad (2)$$

where Ω is the angular rotation rate of the core material and t is time. The final size of the disk is thus very sensitive to the in-fall time and initial angular momentum of the cloud. Numerical models of collapsing molecular clouds, both with and without magnetized cores, have shown that the disks form very rapidly, within approximately 10^4 yr. Molecular cloud core material is dispersed until the disk begins to cool and accretion onto the protostar causes it to begin to lose rather than gain mass [Williams and Cieza, 2011].

Outflows and jets create a cavity in the envelope until only the accreting disk remains of radius ~ 100 AU [Jørgensen et al., 2005]. The gaseous and dusty envelope is then lost and the accretion process slows. The disk transitions from being protostellar to protoplanetary. Eventually kilometer sized objects known as planetesimals form. Disk lifetimes vary from 1-10 Myr before dissipating or becoming debris disks [Williams and Cieza, 2011].

The nearest large star forming regions are the Taurus-Auriga and Rho Ophiuchi molecular cloud complexes, both at a distance of ~ 140 pc [Güdel et al., 2007], but there exists also the much smaller TW Hya association at ~ 50 pc

[Mamajek, 2005]. Taurus-Auriga is primarily a lower mass star formation region as opposed to the Orion nebula, which is also producing massive stars of type O,B and A, while Taurus-Auriga primarily contains M,K,and G class stars and brown dwarfs [Kenyon et al., 2008]. The sun is thought to have formed from a higher-mass star formation region. To explain the prevalence of ^{60}Fe in solar system meteorites the presence of a supernova in the protosolar nebula is invoked and hence that of other higher mass stars [Lee et al., 2008].

Planet Formation

Direct observation of planet formation in the disk is hindered by the optically thick dust and most disks being at distances $>100\text{pc}$, requiring a correspondingly large angular resolution to observe the inner planet forming regions of the disk. For a 200AU diameter disk at 140pc this represents an angular size of $\sim 1.43''$.

1.3 Disk Properties

1.3.1 Disk Mass

PPD mass determinations are still highly uncertain because they cannot rely on a method of direct measurement. Determining the mass of a disk requires a known dust-to-gas ratio (ρ_d/ρ) and the assumption that the disk is optically thin at the relevant wavelengths. For the Milky Way galaxy, a canonical value of $\rho_d/\rho = 10^{-2}$ is adopted [Williams and Cecchi-Pestellini, 2016, Zubko et al., 2004] but several different cases will be treated in the results section of this paper.

Column densities are high in the inner disk and thus continuum emission is optically thick in the near-IR within ~ 10 AU of the star [Guilloteau et al., 2016]. Outside of this radius the disk mass can be related directly to the observed flux F_ν via

$$M = \frac{F_\nu d^2}{\kappa_\nu B_\nu(T)} \quad (3)$$

where d is the distance to the source and for mm observations the RJ approximation for the Planck function becomes valid $B_\nu \equiv 2\nu^2 kT/c^2$. When the radial surface density profile of disks are fit to a power law (from R_{in} to R_c , see section 1.3.2) + exponential taper (beyond R_c to R_{out}) profile the total disk mass can be inferred, although there is still disagreement over the 5-10 AU surface densities [Andrews et al., 2009, Isella et al., 2009] For Class II young stellar objects disks falls off steeply beyond the radius containing the mass $M \sim 50M_J$ [Williams and Cieza, 2011].

Tracers to infer the gas mass independently of the dust mass are the line luminosities of CO and its isotopologues ^{13}CO and C^{18}O [Miotello et al., 2016]. CO is the second most common molecule after H_2 and has very strong rotational and ro-vibrational (which require much higher gas temperature) transitions over a wide range of corresponding temperatures which allows for characterization of different regions in the disk [van der Plas et al., 2015]. The bulk of the gas constitutes H_2 and He, other elements make up only 0.01% of the gas mass. H_2 is not used as a gas tracer because it has no permanent dipole and thus its

emission lines are very weak, and the excitation temperature for these lines is very high. Thus H_2 only probes the gas which is at several 100K and not the majority of the disk gas mass.

Disk masses have been measured in the range 10^{-4} - $10^{-1} M_\odot$ with a lognormal distribution [Andrews et al., 2013]. A linear $M_{disk} \propto M_\star$ has been found with a typical disk to star mass ratio of ~ 0.2 - 0.6% although the influence of different evolutionary states of the disk, dust opacity, and disk temperature could be the cause of the very large spread in inferred disk masses [Andrews et al., 2013].

1.3.2 Disk Size

One issue is finding a general definition for what constitutes the size of a disk. The critical radius R_c has been defined as the radius where the disk surface density begins an exponential drop-off [Andrews et al., 2013].

Disk R_c of 10 to 100's of AU have been observed [Andrews et al., 2013]. Another issue is that the sizes of individual disks are often poorly constrained due to limitations of the tracer used; the gas disk could be more extended than the dust component of the disk, and orientation of the disk relative to the observer, disks viewed edge on exhibit self-shadowing which can cause erroneous continuum flux inferences.

Studies of proplyds in Orion by HST show radii in the range ~ 50 - 200 AU but also up to ~ 620 AU with a median value of 75 AU [Vicente, S. M. and Alves, J., 2005]. Note that proplyds differ from PPDs in being ionized and in the process of being photoevaporated by OB stars, and contain PPDs within them.

[Isella et al., 2009] found for 11 disks in Taurus-Auriga $R_c = 30$ - 230 AU, and that older disks tended to be larger. [Andrews et al., 2009] found $R_c = 14$ - 198 AU for 16 disks in Ophiuchus with an inferred correlation of disk mass $M_d \propto R_c^{1.6 \pm 0.3}$.

Much larger disk sizes are rarely observed as they are often truncated by gravitational interaction with other young stars in a densely populated star forming region or by binary companions [Artymowicz and Lubow, 1994].

1.3.3 Vertical and Radial Structure

While some of the earliest analytical disk models considered geometrically flat disks, it is currently understood that disks can exhibit a "flared" structure. Infrared excesses which could not be explained by a flat disk were discovered by IRAS [Kenyon and Hartmann, 1987]. Such flared disks have been directly imaged in Taurus [Burrows et al., 1996]. The hydrostatic balance equation of the vertical structure of the disk can be approximated as

$$\frac{\partial p}{\partial z} = -\rho \frac{GM}{r^3} z \equiv -\rho \Omega^2 z \quad (4)$$

with p the pressure, ρ the density, G the gravitational constant, M the mass, r the radius, $\Omega = \sqrt{GM_s/r^3}$ Where the solution to the differential equation and with the definition of a pressure scale height H as

$$H = \frac{c_s}{\Omega_K} \quad (5)$$

For a temperature profile of an inverse-square law irradiated disk $T \propto r^{-1/2}$ and $c_s \propto r^{-1/4}$, so that $H \propto r^{5/4}$, and finally $H/r \propto r^{1/4}$. This shows that disk vertical height increases with r to create the flared shape. Values of H/r are typically on the order 10^{-2} and thus geometrically still quite flat.

1.3.4 Content and Chemistry

PPDs are composed of dust and gas. Dust dominates the opacity and supplies the raw material for planetesimal formation. The dust itself is composed of silicates, graphite, and extremely small carbonaceous particles: polycyclic aromatic hydrocarbons (PAHs). Dust grains are the sites for the freezing-out or condensation of volatiles into ice which form icy mantles [Draine, 2011].

Following from the canonical $\rho_d/\rho = 10^{-2}$ gas makes up most of the PPD mass. Despite this the gas is harder to detect, and was detected only after dust around other stars, owing to its emission at only specific wavelengths and thus the need for high resolution spectroscopy. The most abundant species is H_2 . Because of the optically thick dust, only the top of the disk surface is probed by observations of gas which infer only a small fraction the true mass in the MIR.

The main chemical processes which occur in PPDs are photochemistry, molecular-ion reactions, neutral-neutral reactions, gas-grain interactions, and grain surface interactions.

Radial Differentiation

Beyond a certain radius from the star the gas temperature in the disk midplane falls below that required for water ice condensation. This distance is known as the "Snow Line" as gaseous H_2O condenses onto dust grains, increasing their surface density and possibly driving planetesimal growth [Lecar et al., 2006]. Other volatiles such as NH_3 each have their corresponding snow- or frost-lines. Within 0.07-0.15 AU of a typical T Tauri star the irradiation is sufficient for dust to sublimate at temperatures 1500-2000K [Anthonioz et al., 2015]. The most productive planet forming region of the disk is considered to extend radially outwards from the star to a distance of ~ 40 AU [Andrews et al., 2010].

Vertical Stratification

A PPD can be divided vertically into three chemically distinct regions. The surface of the disk is photon dominated. It is directly irradiated by stellar UV which can photodissociate molecules and ionize atoms. The temperature is 10^3 K; elements present in this layer are O,C,C+,N,H.

Below this layer is a warm molecular layer with gas at $T > 100$ K. In this layer can be found H_2O , CO, HCN, OH, H_2 and N_2 [Lahuis et al., 2006, Bast et al., 2013]. In the mid plane of the disk is the cold layer in which volatiles can condense. More complex chemistry is enabled on the surface of the dust grains.

Abundance of molecules relative to H_2 is $10^{-10} - 10^{-4}$. Heavier molecules (such as HC_3N) are not easily detected due to low abundance and weak lines due to energy partitioning between many modes.

1.4 Emission Lines in Disks

1.4.1 Emission Mechanisms and Energy Levels

Rotors

Molecules are free to rotate about three mutually orthogonal axes with origin at the molecule's center of mass, and thus they have three corresponding moments of inertia about those axes. The form of a molecule's emission spectrum is dependent on its energy levels. The allowable energy levels are defined by the symmetry of the molecule. There are four divisions based on symmetry.

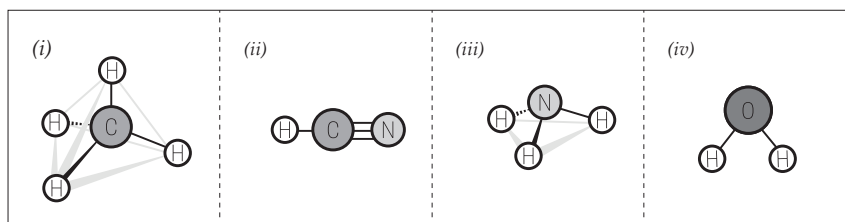


Figure 2: Schematic representation showing examples of the four types of molecular rotors (image credit Silke Ceulemans).

Spherical top molecules ((i) in Figure 2) such as CH_4 and SiH_4 , where all three moments of inertia are equal. Linear molecules ((ii) in Figure 2) O_2 , CO , OH , CO_2 and HCN have one moment of inertia I which is approximated as zero (along its axis of symmetry) and two other moments of inertia which are equal. Symmetric top molecules ((iii) in Figure 2) such as NH_3 , for which any two moments of inertia can be the same. Asymmetric top molecules ((iv) in Figure 2) such as H_2O have three moments of inertia with three different values.

Rotational Transitions

Photon emission occurs during the relaxation of an atom or molecule from one quantized energy level to a lower one. The emitted photon energy is equal to the difference in energy between the energy levels. In the mid-infrared many ro-vibrational lines of elements in the gas phase are present.

The rotation rates of molecules about any of their mutually orthogonal rotational axes are discretized following from the quantization of angular momentum. The orbital angular momentum L exists in multiples of $\hbar = h/(2\pi)$ [Hol, 2005].

$$L = n\hbar \quad (6)$$

Free molecules rotate about their center of mass. In an inertial center of mass frame $L = I\omega$ where I is the moment of inertia and ω is the angular velocity. This can be written in terms of the equilibrium distance r_e , the distance separating the mass of the two atoms, and their total mass m as

$$L = mr_e^2\omega \quad (7)$$

The rotational kinetic energy is related to the angular momentum and moment of inertia by $E_{rot} = L^2/2I$. The relation between L and J is thus $L = \sqrt{J(J+1)}\hbar$, so

$$E_{rot} = \frac{J(J+1)\hbar^2}{2I} \quad J = 0, 1, 2, \dots \quad (8)$$

The energy levels of linear molecules are described by a single moment of inertia and thus single quantum number J . Nonlinear symmetric rotor molecules have two unique moments of inertia and so their energy depends also on a second rotational quantum number K . Not only the energy itself but also changes in rotational energy are quantized $\Delta J = \pm 1$. The frequency of emitted photons is thus

$$\nu = \frac{\hbar(J+1)}{2\pi I} \quad J = 1, 2, \dots \quad (9)$$

Hence rotational line emission frequencies exist in a 'ladder' of steps. Each step on the ladder signifies a different J level of a rotating molecule [Hol, 2005]. A diatomic molecule such as H_2 is linear and has only one rotational degree of freedom. The nonlinear symmetric top molecule NH_3 has two distinct rotational axes and their coupling causes more complex spectra with multiple 'ladders' of different step spacing. The energy of the transitions of rotating molecules such as H_2O fall in the mid-infrared range [Hol, 2005].

Vibrational Transitions

Molecular vibrations can be approximated to first order by simple harmonic oscillators. Solving the Schrödinger equation for the energy levels leads to

$$E_n = h\left(v + \frac{1}{2}\right)\nu \quad (10)$$

where v is the vibrational quantum number and $\nu = \sqrt{k/4m\pi^2}$ the vibrational frequency. For this approximation the selection rules for permitted transitions allow $\Delta v = \pm 1$ but in reality vibrations are anharmonic and there are additional contributions from e.g. $\Delta v = \pm 2, 3$ etc [Hol, 2005]. In astronomical nomenclature, lines arising from vibrational transitions where both states have the same rotational quantum number ($\Delta J = 0$) form the Q-branch. The R-branch of the spectrum arises from rotational transitions of $\Delta J = +1$. The P-branch forms from rotational transitions of $\Delta J = -1$. The relative excitation energies for rotational, vibrational, and electronic transitions are related by the inequality

$$E_{rot} \ll E_{vib} \ll E_{el} \quad (11)$$

1.4.2 Gas Emission

Stellar radiation causes pronounced gas excitation and ionization in the surface and inner radii of the disk ($R < 10AU$). Even if a disk is spatially unresolved, the location of gas emission can still be inferred. The gas in the disk is expected to follow a Keplerian rotation profile and thus the doppler broadening of a particular line can be an indicator of its radial location in the disk. For a disk of inclination θ the radial position R of a line can be determined by the relation

$$R = R_{out} \left(\frac{u_{out}}{u} \right)^2 \cos^2 \theta \quad (12)$$

where u is the velocity vector along the line of sight, R_{out} is the outer disk radius, and u_{out} is the velocity at that outer radius. Line profiles become double peaked, but a spectral resolution which can resolve the line splitting is required.

CO ro-vibrational emission from a typical T Tauri PPD could originate from ~ 0.1 -10AU for which the expected keplerian velocity on a circular orbit would be ~ 50 -5km/s respectively. A line of sight velocity of 50km/s represents a doppler shift of $\sim 0.0008 \mu\text{m}$, hence a split peak would be separated by $\sim 0.0016 \mu\text{m}$ and require a spectral resolution of $R = 2900$ to be resolved.

1.4.3 Dust Emission

Thermal emission from the star and the dust grains in the disk makes up the continuum flux. Thermal emission of dust grains at a temperature of 100-500K falls in the ~ 6 -30 μm range, a region known as the mid-IR. The grains are heated predominantly by photons, with additional contributions from collisional processes. The grains can become excited by absorbing an incident photon and are heated by the photon energy going into vibrational energy modes. The grain will then cool primarily by emitting an IR photon, but can also cool by collisional de-excitation in denser regions or through the sublimation of atoms from the grain surface [Draine, 2011].

1.4.4 The MIR Organic Spectrum

The first detection of organics in PPDs was made in 2008 including HCN, C₂H₂ and CO₂ in AA Tau and then in other classical T Tauri stars [Carr and Najita, 2011]. The inferred temperature (T=200-800K) of detected species correspond to the emission coming from inner planet-forming region. Some prominent lines include the Q branches at 13.7 μm , 14 μm and 14.95 μm . Q branch HCN and C₂H₂ is detected in 67% and 44% of the surveyed disks.

The vast majority of lines in the Spitzer MIR range are rotational transitions of the main H₂O isotopologue H₂¹⁶O [Williams and Cieza, 2011]. Strong blends include

1.5 Stars with Disks

Protoplanetary disks are found around >90% stars with age <1Myr, 50% of stars with age ~ 2 Myr, and by ~ 15 -20Myr virtually all disks are absent [Mamajek, 2009]. Pre-main sequence (pre-MS) stars with a mass <2M_⊙ are known as T Tauri (TT) stars [Bertout, 1989], first described by Alfred Joy in 1945 [Kuhi, 1966] most of which are surrounded by sufficiently massive disks [Williams and Cieza, 2011] to host planet formation [Greaves, 2004]. They are the youngest stars of class M,K,G and F. Their luminosity is dominated by their gravitational collapse prior to the ignition of hydrogen fusion as they move along a Hayashi track [Kuhi, 1966]. After 10⁸ yr of evolution these stars reach the main sequence. T Tauri stars can be identified by strong [Li I] 0.6707 μm absorption [Bertout, 1989] which is present for typically < 10⁷ yr [Mamajek, 2009]. More massive pre-MS stars of 2-8M_⊙ of type A and B are known as Herbig Ae/Be type stars.

1.5.1 FT Tauri in Taurus-Auriga

FT Tauri (FT Tau) is a ~ 1.6 Myr old star of spectral class M2 or M3 with a protoplanetary disk. The star has a mass $\sim 0.3 M_{\odot}$, a radius $1.7R_{\odot}$ and a luminosity $\sim 0.35L_{\odot}$ [Garufi et al., 2016] which are typical values for a T Tauri star. The disk has a mass of $0.02 M_{\odot}$ and extends from 0.05-200AU with a flaring power law exponent 1.15. The star and disk are considered a benchmark for high mass accretion rate and high gas content systems.

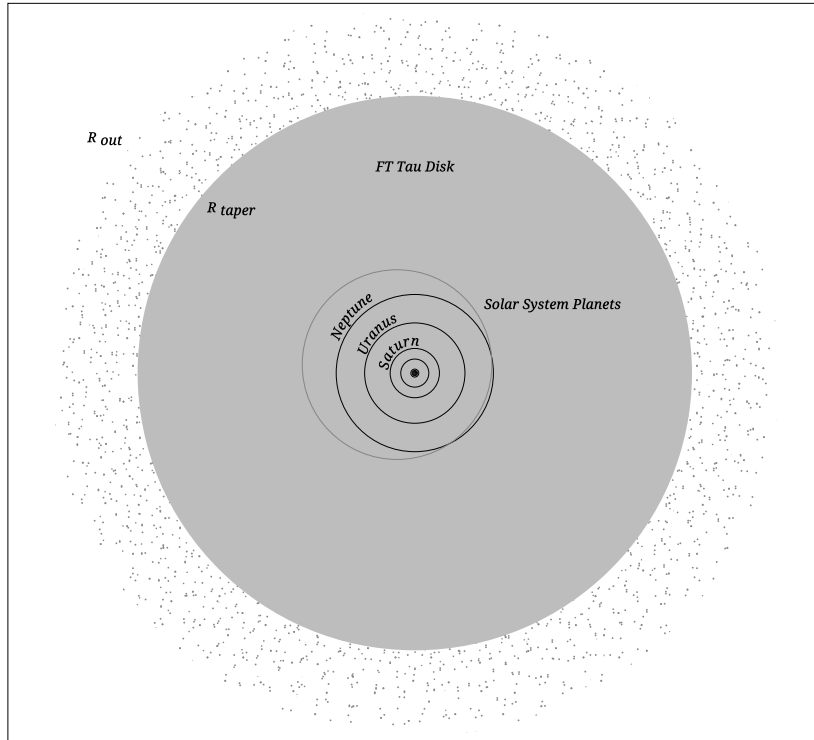


Figure 3: Simplified schematic representation of the disk of FT Tauri compared to the orbits of the planets of the solar system. The parameters R_{out} and R_{taper} are explained in section 2.8.1 (image credit Nick Oberg and Silke Ceulemans).

FT Tau is located in Taurus south of the $400^{\circ}2$ Barnard 215 dark cloud, where it is the only known member of Taurus besides the binary brown dwarf pair FU Tau A and B which were discovered during a *Spitzer* observation of FT Tau in 2005 [Luhman et al., 2009].

1.6 MIRI

The Mid-Infrared Instrument (MIRI) will fly aboard the James Webb space telescope when it is launched into space by an Ariane 5. It will then coast out to an orbit about the Earth-Sun Lagrange point L2 from which it will make mid-infrared observations of unprecedented spectral resolution for this wavelength range.

The large thermal background from the Earth’s atmosphere (T=288K) makes ground based MIR observations impossible, and requires space telescopes such as IRAS, ISO, *Spitzer*, *Akari*, WISE and JWST which are equipped with specialized cryogenic equipment. To fall within the mass and volume constraints for most available space launch vehicles the telescopes have all had small apertures (40-85cm) compared to ground based telescopes [Rieke et al., 2015].

MIRI contains an integral field Medium Resolution Spectrometer (MRS) with a spectral resolving power R given by

$$R = \frac{\lambda}{\Delta\lambda} \quad (13)$$

ranging from 1300 to 3700 over 5 to 28.5 μm with a field of view up to 7.7 x 7.7 arcseconds [Wells et al., 2015]. The short wavelength radiative background below 5 μm is dominated by zodiacal dust emission. Above 17 μm thermal emission from the telescope and straylight begins to dominate and cause the long wavelength limit [Glasse et al., 2015]. The gain in sensitivity over *Spitzer* in the range 5-12 μm is a factor of ~ 50 [Rieke et al., 2015]. Four integral field units (IFU) divide the spectral range within the spectrometer pre-optics into 4 simultaneous ranges. The IFUs are image slicers which reformat the input field for presentation to a grating spectrometer [Wells et al., 2015].

Table 1: MIRI Spectral Resolution in Detail

Channel	1	2	3	4
	Sub-band A			
Wavelength Range (μm)	4.87-5.82	7.45-8.90	11.47-13.67	17.54-21.10
Resolution ($\lambda/\Delta\lambda$)	3320-3710	2990-3110	2530-2880	1460-1930
	Sub-band B			
Wavelength Range (μm)	5.62-6.73	8.61-10.28	13.25-15.80	20.44-24.72
Resolution ($\lambda/\Delta\lambda$)	3190-3750	2750-3170	1790-2640	1680-1770
	Sub-band C			
Wavelength Range (μm)	6.49-7.76	9.91-11.87	15.30-18.24	23.84-28.82
Resolution ($\lambda/\Delta\lambda$)	3100-3610	2860-3300	1980-2790	1630-1330

This separation allows for the diffraction gratings to be used in first order, such that they are used near peak efficiency around the blaze wavelength. [Wells et al., 2015] Two focal planes of 1024x1024 Si:As detectors record the output with a spectral coverage of roughly one third of the wavelength range of each channel [Ressler et al., 2015].

1.7 Significance

The study of protoplanetary disks is motivated by a desire to understand the prevalence and conditions of planet formation. The habitability of planets is currently assessed with simple arguments based on stellar flux [Kopparapu et al., 2013] and broad generalizations of composition must be made for the few exoplanets with a known mass and radius [Weiss and Marcy, 2014]. With a better

understanding of the inner region of protoplanetary disks we may be able to make inferences regarding the distribution of planet compositions. Perhaps most intriguingly the evolution of pre-biotic chemistry in disks can be explored [Snytnikov et al., 2014]. JWST/MIRI will an overview of molecular species in the inner planet forming regions of disks, a task which forced *Spitzer* to the limits of its capability. This thesis aims to provide estimates for the performance of MIRI with regard to PPDs. It will draw from both theoretical simulation and observational data to present a MIR spectrum representative of the star FT Tau with which MIRI's performance can be evaluated and its observations planned in advance.

2 Modeling Disks

2.1 ProDiMo

The disk modeling in this paper was performed with the ProDiMo (**P**rotoplanetary **D**isk **M**odel) FORTRAN 90 software package [Woitke et al., 2009]. ProDiMo models the physical and chemical structures and heating/cooling of the disk gas using global iterations. From a parametrized disk structure a continuum radiative transfer solution is calculated with sub-iterations of dust temperature distribution, from which a chemistry and gas thermal balance is calculated with sub-iterations of gas temperature, and finally sound speeds.

Thus ProDiMo combines 2D dust continuum radiative transfer, kinetic gas-phase and UV photo-chemistry, ice formation, and detailed non-LTE heating and cooling [Woitke et al., 2009].

2.2 ProDiMo Disk Structure

In this thesis the ProDiMo disk structure is parametrized by a radial column density power law and flaring-radius relation. An inner radius R_{in} , outer radius R_{out} , and tapering radius R_{tap} (note $R_{\text{out}} \ll R_{\text{tap}}$) are input directly as parameters, giving a gas column density structure $\Sigma(r)$ [g/cm^2]

$$\Sigma(r) \propto r^{-\epsilon} \exp\left(-\left(\frac{r}{R_{\text{tap}}}\right)^{2-\gamma}\right) \quad (14)$$

where r is the radius [Woitke et al., 2016]. The tapering exponent is by default set to be $\gamma = \epsilon$ [Hartmann et al., 1998]. Radial integration of equation 14 from R_{in} to R_{out} results in the total disk mass M_{disk} . R_{taper} is chosen such that at R_{out} the number density of hydrogen N_{H} will be on the order 10^{20}cm^{-2} . The vertical gas distribution is taken to be Gaussian and the input parameters include the tapering exponent γ , column density exponent ϵ , scale height H_g and flaring exponent β ;

$$\rho(r, z) \propto \exp\left(-\frac{z^2}{2H_g r^2}\right) \quad (15)$$

$$H_g(r) = H_0 \left(\frac{r}{r_0}\right)^\beta \quad (16)$$

where $\rho(r, z)$ is the gas mass density in cylindrical coordinates, and H_0 is the gas scale height at radius r_0 .

2.3 ProDiMo Continuum Radiative Transfer

The main purpose of continuum radiative transfer in ProDiMo is to calculate the condition of radiative equilibrium of dust grains and local strength of UV radiation field, from which the dust temperature and UV photo-chemistry rates can be calculated.

The local radiation field $J_\nu(r, z)$ and dust temperature $T_d(r, z)$ determine the chemistry and heating/cooling balance of gas in the disk. Furthermore the chemistry and heating/cooling balance are functions of the heat transfer between the gas and dust (which is the dominant heating and cooling mechanism for dense regions such as the disk midplane), photo-ionization and dissociation and UV heating, radiative pumping of atoms, and grain surface chemistry. [Draine, 2011]

ProDiMo computes a 2D continuum radiative transfer solution for $J_\nu(r, z)$ and $T_d(r, z)$ at each point in the disk. The disk is subdivided into a grid from which ~ 100 rays are traced back along the direction of photon propagation. The radiative transfer equation

$$\frac{dI_\nu}{d\tau_\nu} = S_\nu - I_\nu \quad (17)$$

is then solved for these rays, where I_ν is the spectral radiance, τ_ν the spectral optical depth, and $S_\nu = \epsilon_\nu/\kappa_\nu$, the ratio of emissivity to absorptivity .

2.3.1 Stellar Irradiation

The radiation field around disks is completely determined by the stellar and interstellar radiation, and the dust opacity. A PHOENIX model is used to simulate the stellar radiation. The incident stellar intensity is related to the surface flux at the stellar surface by

$$I_\nu^{star} = \left(\frac{1}{\pi}\right) F_\nu^{star} R_{star} \quad (18)$$

where I_ν^{star} is the stellar intensity, F_ν^{star} is the stellar spectral flux, and R_{star} is the stellar radius.

As younger stars can have a UV excess compared to the model star an additional UV component is added to the model. The UV irradiation of the disk is important for ProDiMo as only the UV photons can drive the ionization and photo-dissociation that are responsible for heating, cooling and chemical processes.

ProDimo assumed a uniform dust abundance and size distribution across the disk. The dust in the ProDiMo simulations in this paper consists of 3 components, an amorphous pyroxene $Mg_{0.7}Fe_{0.3}SiO_3$, amorphous carbon dust, and vacuum at a 0.727:0.023:0.25 ratio by volume.

2.4 ProDiMo Chemistry

There are 9 elements (H,He,C,N,O,Mg,Si,S,Fe) and 71 species (see for a detailed list [Woitke et al., 2009]) in ProDiMo from which any subset can be selected. Reaction rate coefficients are taken from UMIST 2012 astrochemistry database [McElroy et al., 2013]. 950 Reactions are included in ProDiMo of which 74 are photo-reactions, 177 are neutral-neutral reactions, 299 are ion-neutral reactions, 209 are charge-exchange reactions, 46 are cosmic ray induced photo-reactions and 26 three-body reactions. [Woitke et al., 2009]

2.5 ProDiMo Gas Thermal Balance; Heating and Cooling

Heating and cooling rates depend on the gas temperature T_g and the particle densities n_{sp} which themselves depend on T_g , such that an iterative process is required during which T_g is varied and the chemistry is re-solved until T_g satisfies

$$\frac{de}{dt} = \sum_k \Gamma_k (T_g, n_{sp}) - \sum_k \Lambda_k (T_g, n_{sp}) \quad (19)$$

where Γ_k and Λ_k are the heating and cooling rates (in $\text{erg cm}^{-3}\text{s}^{-1}$) and e is the kinetic energy [Woitke et al., 2009].

2.5.1 Heating Processes

UV photons can eject electrons from dust grains which carry their kinetic energy into the disk as heating in a process known as photo electric heating. The electrons collide with gas atoms and molecules and transfer some of their own kinetic energy in those collisions. Positive grain charge reduces the efficiency of this heating as they will be more likely to deflect electrons rather than collide with them. The photoelectric heating rate is taken from [Kamp and Bertoldi, 2000].

Carbon photoionization, H_2 photodissociation heating, cosmic-ray heating, H_2 formation heating, heating by collisional de-excitation of H_2^* and viscous heating are also all included in ProDiMo. In just the inner disk surface region, collisional de-excitation of excited H_2 dominates near the disk surface, and beneath that H_2 formation by grain catalysis, and IR background heating by H_2O ro-vibrational emission are present, as can be seen in Figure 4.

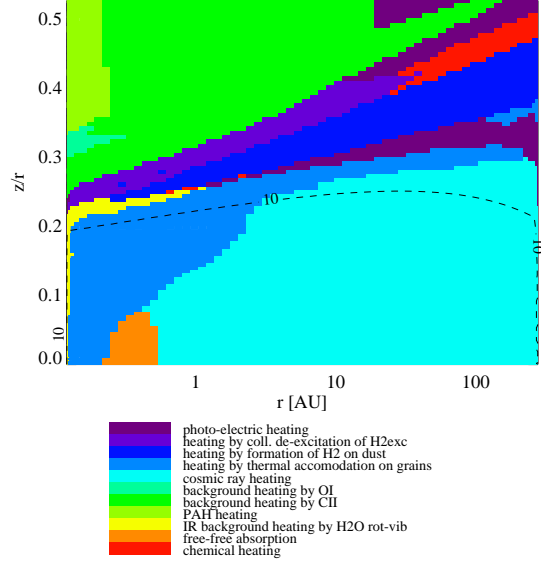


Figure 4: FT Tau disk heating processes as simulated by ProDiMo

2.5.2 Cooling Processes

Major cooling processes in the gas content of the disk are radiative. On the surface of the PPD [CII] $158\mu\text{m}$ cooling dominates, beneath that [OI] 44, 63, and $144\mu\text{m}$. In the disk midplane cooling by thermal accommodation of grains dominates. Closer in to the star there is [FeII],[OI],and CO ro-vibrational cooling. Inside the snow-line there is H_2O rotational and H_2 ro-vibrational cooling as seen in Figure 5.

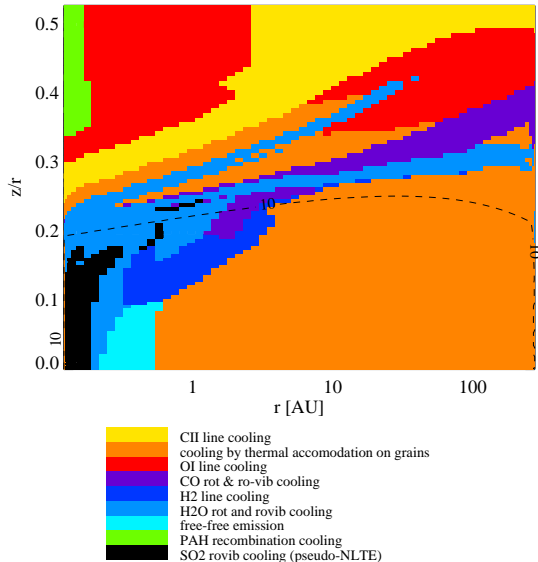


Figure 5: FT Tau disk cooling processes as simulated by ProDiMo

Emission lines are saturated around $\tau = 1$, thus the majority of observable line flux originates from surface regions. In the disk mid plane $\tau \gtrsim 10^6$.

2.6 The Fast Line Tracing System

The inner region of disks from which much of the MIR emission originates is characterized by rapidly varying temperature, density, and composition, requiring a detailed numerical grid. The large number of blended lines in this wavelength range adds to the complexity of the emission line computation and the large velocity gradients across individual grid cells degrade the accuracy of line opacities. Such computation was challenging with the previous generation of line ray-tracers.

The Fast Line Tracing System (FLiTs) was developed by Dr.M.Min (Anton Pannekoek Institute for Astronomy) to address this issue. FLiTs is used in this paper to compute line shapes and fluxes. From ProDiMo a density and temperature structure is imported and FLiTs computes dust and gas emission using the formal solution of radiative transfer. Species selection is modular, individual species or combinations of species can be selected.

An image of the disk is created by ray tracing radiation along different lines of sight. The contributions from each line of sight are combined to obtain a total flux at each wavelength. The flux contribution is solved by integrating along the line of sight using a discretization of the disk volume.

Spectra must be calculated at high spectral resolution in FLiTs to resolve lines and only then can be re-sampled to simulate lower spectral resolutions. FLiTs was recently developed within the DIANA project. DIANA (Disc Anal-

ysis), an EU project funded under the FP7 program (Grant Agreement no. 284405, PI: P. Woitke).

2.7 Noise and Spectral Resolving Power Simulation

Noise which is artificially added to synthetic spectra for comparison with *Spitzer* is approximated as

$$N = 0.01r_n F_c \quad (20)$$

where r_n is a random number drawn from a normal distribution centered on zero with a standard deviation of one and F_c is the continuum flux [Antonellini et al., 2016]

Table 2: MIRI Spectral Resolution Approximation

Wavelength [μm]	Resolution
4.910-5.695	3200
5.695-6.540	3150
6.540-7.590	3000
7.590-8.810	2750
8.810-10.115	2700
10.115-11.605	2800
11.605-13.390	2450
13.390-15.490	2000
15.490-18.010	2100
18.010-21.015	1500
21.015-24.255	1550
24.255-27.430	1350

The spectral resolution R of MIRI is approximated by taking the mean R over each of the 12 sub-band wavelength ranges [Wells et al., 2015]. See Table 2.

2.8 MIRI sensitivity estimation

Sensitivity estimates for MIRI MRS are derived from Figure 10 in [Glasse et al., 2015]. This plot has been digitized and converted to spectral flux density (Jy) and interpolated with a polynomial fit. Originally it is designed to return detection criteria for unresolved spectral lines from a spatially unresolved source for a 10σ detection after 10,000s of observation.

This relation has been altered to account for 3 sigma detections of much shorter exposure times, namely $\sim 20\text{s}$ and $\sim 200\text{s}$. Namely the required flux for a detection of 10σ after 10,000s, F has been decreased by a factor $3/10$ to change the significance criterion and by a factor $\sqrt{10000/20}$ to adjust the exposure time SNR (for 20s exposure) as $\text{SNR} \propto t^{0.5}$.

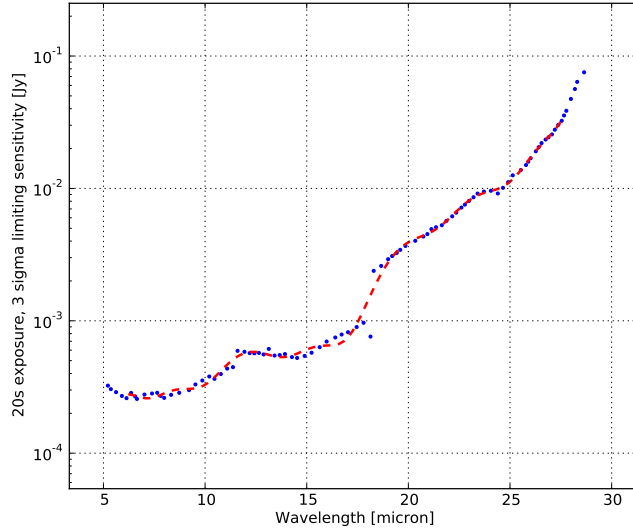


Figure 6: The MIRI MRS limiting sensitivity for a 20s exposure, 3σ detection as a function of wavelength, derived from [Glasse et al., 2015]

2.8.1 FT Tau as parametrized in ProDiMo

The parameters in Table 3 were used for the reference simulation of FT Tau in ProDiMo, and are taken from a modified DIANA standard set of FT Tau parameters. These parameters were initially derived from a multi-wavelength analysis and modeling of FT Tau [Garufi et al., 2016]. Data from TNG/DOLoRes, WHT/LIRIS, NOT/NOTCam, Keck/NIRSpec, and *Herschel*/PACS were collated to form a complete spectral energy distribution (SED) and replicated with ProDiMo and *MCFOST* to constrain the properties of the disk [Garufi et al., 2016].

Table 3: FT Tau Stellar Parameters

Parameter	Value
Stellar Mass [M_{\odot}]	0.3
Stellar Luminosity [L_{\odot}]	0.2954
Stellar Effective T [K]	3400
LUV/Lstar	0.025
UV powerlaw exponent	0.2
X-ray Luminosity [erg/s]	1E20
X-ray Temperature [K]	2E7

The significant deviation in disk mass in Table 4 from $M_{disk} = 0.02 M_{\odot}$ found by the study versus the value $M_{disk} = 0.37M_{\odot}$ used here arises from a

new DIANA modeling approach, which adopts a more realistic opacity model rather than one based on astrosilicates for the dust. The disk models is now parametrized with a tapered rather than sharp outer edge.

Table 4: FT Tau Disk Parameters

Parameter	Value
Disk Mass [M_{\odot}]	0.371
R_{in} [AU]	0.12
R_{taper} [AU]	105.6
R_{out} [AU]	138.4
ρ_d/ρ	0.01
γ (tapering)	1.6
ϵ (column density exponent)	1.1
β (flaring power)	1.12
H_0 (scale height)	9.1

3 Results

26 ProDiMo disk simulations including 4 different parameter space explorations were performed. 150 FLiTs simulations of both individual and multiple species were performed to generate spectra of $R = 30000$.

3.1 Comparing ProDiMo+FLiTs and Spitzer

A spectrum of FT Tau acquired by Spitzer on the wavelength range ~ 10 - $20 \mu\text{m}$ is considered. The inherent spectral resolution of *Spitzer's* Infrared Spectrograph (IRS) over this range is ~ 600 . The FT Tau spectrum is acquired by the 10- $19.5 \mu\text{m}$ and 19- $37 \mu\text{m}$ high-resolution modules. The spectrum has been reduced in such a way to present a higher sampling of lines equivalent to a resolving power of $R = 1200$.

The first FLiTs spectrum was computed with ProDiMo's output using the parameters from Table 3 and Table 4. Thereafter the full 4- $30 \mu\text{m}$ wavelength range was simulated at a spectral resolution of $R=30000$ in FLiTs using the species C+, O, C, Mg+, Fe+, Si+, S+, o-H₂, p-H₂, CO, o-H₂O, p-H₂O, ¹³CO, OH, SiO, NO, S, HCN, CN, HCO+, CH+, N+, OH, Ne+, SO, SO₂, o-H₃O+, p-H₃O+, H, o-NH₃, p-NH₃, Ar+, Ar++, O++, O+, S++, Ne++, N++, C¹⁸O, N₂H+, CO+, OH+, O₂, C¹⁷O, NO, CO₂, and CH₄.

The FLiTs spectrum was then binned to approximate the spectral resolution of *Spitzer*. This was accomplished with a custom python script which takes a Riemann sum approach to integrate the spectra while conserving line flux during the binning process. The binned FLiTs spectra are not binned to simulate $R=600$ and then re-sampled to match the appearance of the *Spitzer* spectra (which would be cosmetic, lacking further insight into the *Spitzer* data reduction process), but rather binned directly at the equivalent sampling rate $R = 1200$ to avoid a potentially misleading result.

A comparison of this simulated spectrum and the *Spitzer* spectrum can be seen in Figure 7 which shows a continuum spectral flux density excess over *Spitzer* from 17-19 μm and beyond 20 μm which continues to increase at longer wavelengths, and a deficit from 13.5-16.5 μm . Thus in the regions 17-19 μm and $> 20\mu\text{m}$ the line/continuum ratio for the *Spitzer* spectrum will be increased by a factor 1.06 over ProDiMo+FLiTs for line fluxes which could in absolute terms be identical, and up 1.12 for the long wavelength end of the spectrum. For the region 13.5-16.5 μm the reverse is true. This is treated in the discussion section.

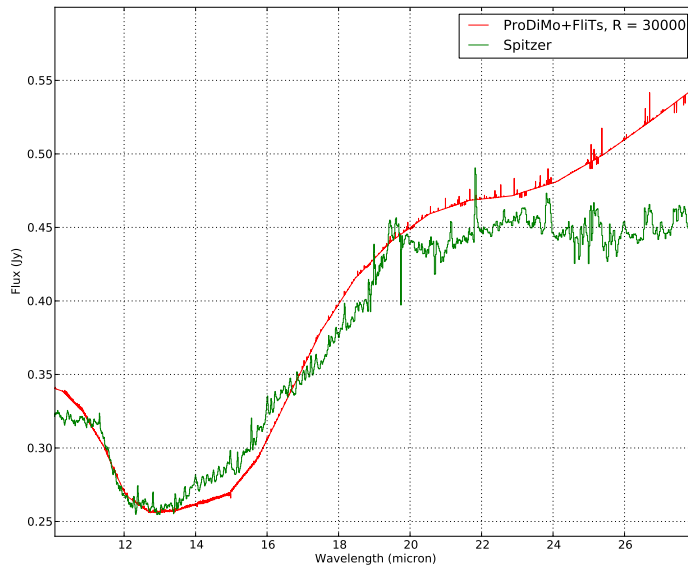
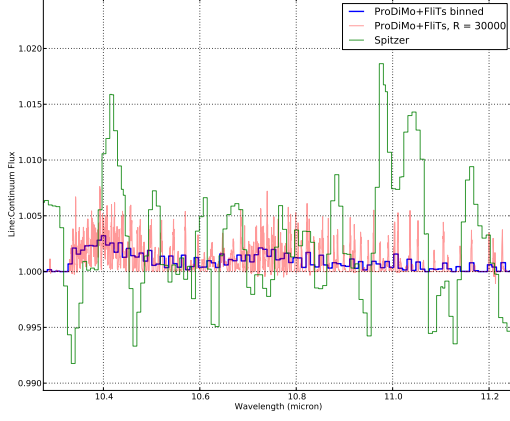
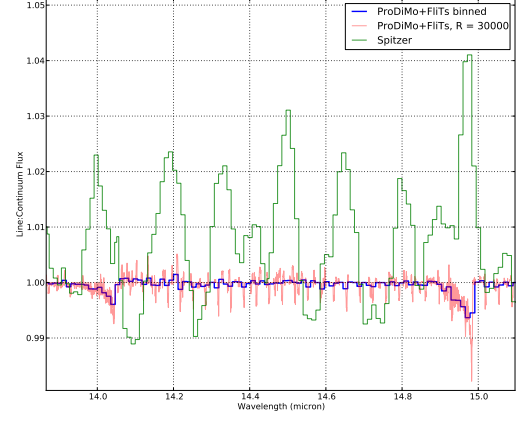


Figure 7: Spectral flux density of the ideal DIANA FT Tau ProDiMo+FLiTs and *Spitzer*. The MIRI-relevant overlap region covers 10-28 μm .

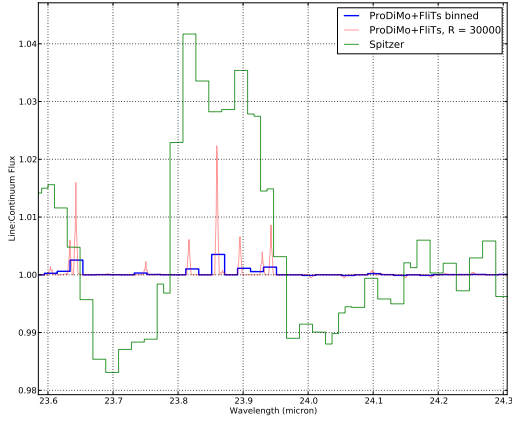
Prior to generating a detailed and representative MIRI-like spectrum for FT Tau, we explore a parameter space in an attempt to bring the continuum and line flux of the ProDiMo and FLiTs output into the same order as that of the *Spitzer* spectrum, but it is not yet clear whether this is possible with physical disk parameters. We adjust the abundance of PAHs, the chemical heating efficiency, the H₂ cosmic ray ionization rate, the gas mass and ρ_d/ρ ratio, and finally as an informative exercise the stellar parameters.



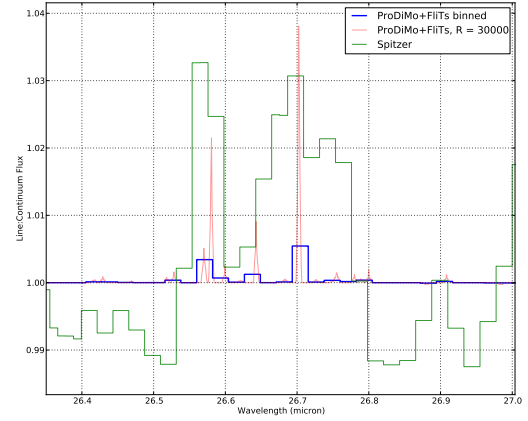
(a) Ammonia band at 10.3-11.2 μm



(b) HCN and CO₂ absorption



(c) H₂O band at 24 μm



(d) H₂O band at 26-27 μm

Figure 8: Initial comparison of continuum normalized, noise-free DIANA standard FT Tau ProDiMo+FLiTs and continuum normalized *Spitzer* Spectrum

Initially the ProDiMo+FLiTs spectrum line fluxes used for comparison (visually inspected bright and isolated H₂O lines at the long wavelength end of the range) are clearly below the *Spitzer* lines visible in Figure 8. To quantify this, several of the water lines are considered. Under the assumption that the 3σ emission which correspond to H₂O line positions are real detections by *Spitzer* and that the *Spitzer* SNR ≈ 100 , the relative line flux between *Spitzer* and ProDiMo+FLiTs is calculated at 23.85, 25.05, 25.35, 26.0, 26.6, and 26.7 μm [Antonellini et al., 2016]. This results in range of ratios from a low of factor 2.7 to a high of factor 76.8. The mean of these ratios is, taking into account the continuum discrepancies at wavelengths above 20 μm is ~ 20 , and this factor will be the working hypothesis for the remainder of the thesis. The total integrated

continuum normalized line flux over the entire *Spitzer* and FLiTs+ProDiMo overlapping wavelengths range is not considered as the continuum flux as inferred from *Spitzer* data and as modeled by FLiTs+ProDiMo is too different for a simple quantitative comparison.

First the simplified model of noise (see equation 20) is applied to the spectra (see Figure 9). The mean continuum flux to line flux ratio for each line traced by FLiTs of the DIANA FT Tau model for ProDiMo+FLiTs output is $\sim 8000:1$, so virtually all lines are completely lost in the noise.

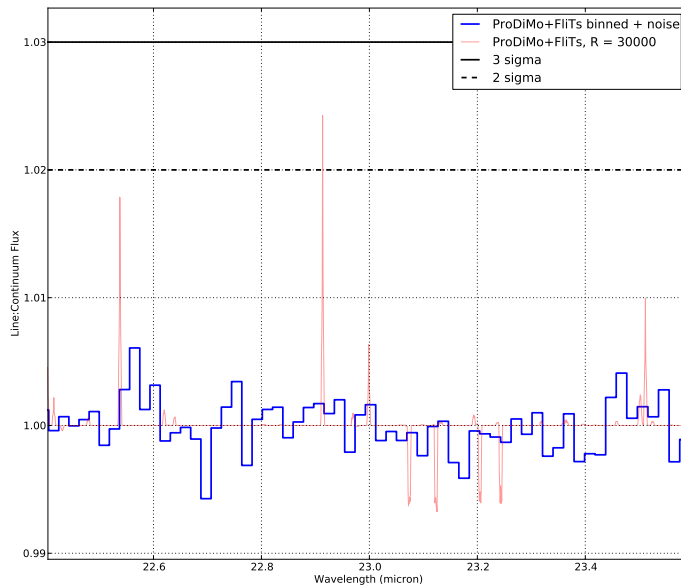


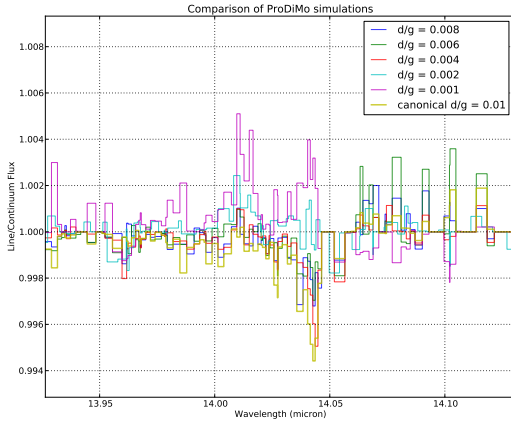
Figure 9: The continuum normalized DIANA FT Tau ProDiMo+FLiTs spectrum with synthetic noise. The signal appears lost in the noise.

3.1.1 ProDiMo M_{gas} parameter exploration

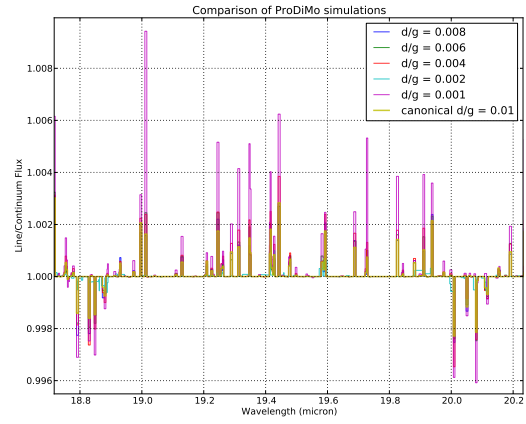
In the first series we alter the disk gas content total mass to investigate the effects it will have on the line flux. FT Tau is already known to have a massive disk, with ratio $M_{\text{disk}}/M_{\text{star}} = 1.23$, greater than the proportionality $\sim 0.02-0.06$ found by [Andrews et al., 2013], despite this we consider a series of disks some of which are almost certainly non-physical, where the disk mass not only exceeds this ratio but significantly exceeds the mass of the star FT Tau itself by up to a factor 12.4. Unfortunately very few disks have had an inferred mass of even $0.1M_{\text{star}}$, so each of the 6 tests should be considered to represent either abnormally massive or completely non-physical disks [Andrews et al., 2013]. To test this the ρ_d/ρ ratio and disk mass is altered to keep dust mass and thus continuum flux fixed.

Simulation	dg1	dg2	dg3	dg4	dg5	dg6
Disk Mass [M_{\odot}]	0.1	0.46	0.617	0.925	1.85	3.71
Ratio M_{dust}/M_{gas}	0.037	0.008	0.006	0.004	0.002	0.001
Ratio M_{disk}/M_{\star}	0.33	1.54	2.04	2.94	6.25	
LBF*	0.39	1.13	1.26	1.44	1.79	2.72

*Line Boost Factor = continuum normalized integrated line flux of test simulation divided by baseline simulation.



(a) $14\mu\text{m}$ HCN band reversal



(b) Significant boost in H_2O lines

Figure 10: Detail of M_{gas} series.

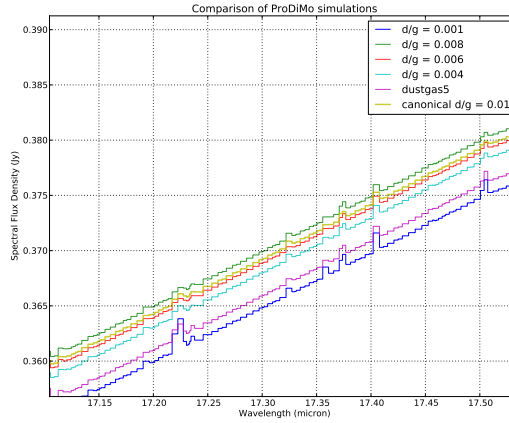


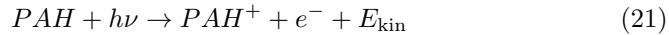
Figure 11: M_{gas} series continuum shifts.

Most observed gas emission from PPDs originates only from the optically thin surface layer. The maximal increase in M_{gas} in series dg6 resulted in a mean

boosting of the continuum normalized integrated line flux over the entire 4-30 μ m range by a factor 2.72, reducing the discrepancy of the reference simulation and Spitzer’s but not eliminating it.

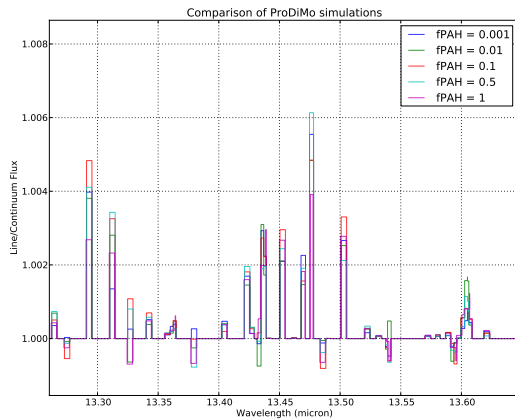
3.1.2 ProDiMo PAH abundance parameter exploration

ProDiMo allows for a change in the abundance of PAHs in the PPD. The f_{PAH} parameters sets this abundance relative to PAH abundance in the ISM. PAHs in this simulation (and all others) were not included in the radiative transfer calculation of ProDiMo such as not to change the fit FT Tau SED. PAHs can influence the heating rate in the disk via photoelectric emission of an electron and are considered an extremely efficient heating source for the gas [Woitke et al., 2009]

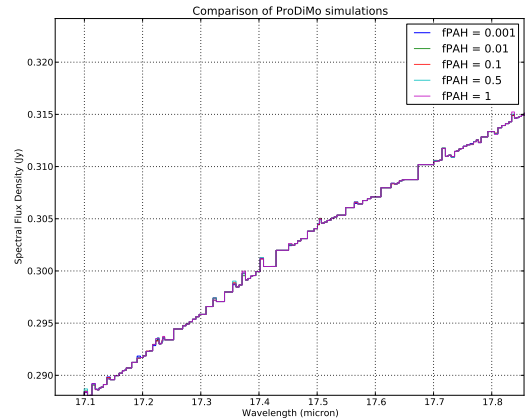


The kinetic energy of the electron which appears on the RHS of equation 21 is carried away into the disk and thermalized. In this series of simulations the dust continuum radiative transfer was not calculated. A series of values for this parameter are considered where a value of $f_{\text{PAH}} = 1$ is equivalent to ISM PAH abundance:

Simulation	pah1	pah2	pah3	pah4	pah5
f_{PAH}	0.001	0.01	0.1	0.5	1



(a) Continuum normalized line fluxes.



(b) No shift in continuum emission.

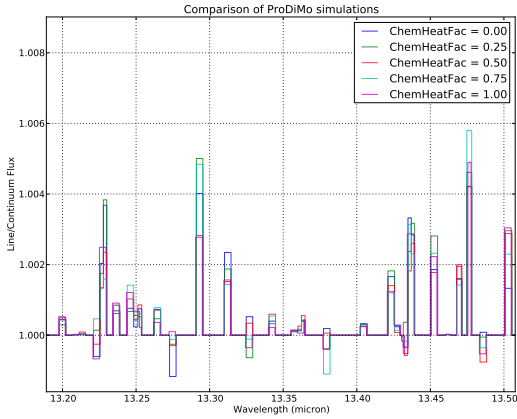
Figure 12: Detail of PAH abundance series.

As seen in plot (a) of Figure 12 the line fluxes do not appear to be uniformly and systematically influenced by the changing PAH abundance. While the continuum flux has remained unaffected.

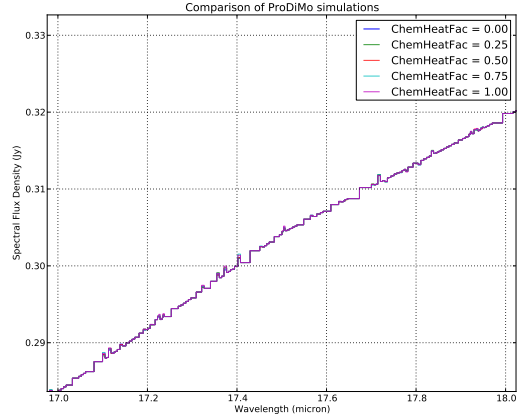
3.1.3 ProDiMo chemical heating efficiency parameter exploration

In an ideal kinetic chemical equilibrium there would be no net formation or destruction of chemical species, but the chemistry would be powered by never ending reaction cycles driven by incoming XUV photons and cosmic rays. Stable molecules are struck by these high energy photons and protons and either ionized or dissociated. The dissociated fragments are energetically less favorable and will re-form into the stable configurations. The majority of these reactions are exothermic and release heat into the gas [Woitke et al., 2016]. This heating mechanism is particularly important in the bottom of the warm molecular layer where near-mid IR lines are formed, and so this parameter is quite relevant to increasing MIR line flux. In this series of simulations the dust continuum radiative transfer was not calculated. The DIANA FT Tau value for this parameter is 0.2.

Simulation	chem1	chem2	chem3	chem4	chem5
ChemHeatFac	0	0.25	0.5	0.75	1



(a) Continuum normalized line fluxes.



(b) No shift in continuum emission.

Figure 13: Detail of chemical heating efficiency series.

Once more the continuum flux remains unchanged. Some lines do appear to increase in flux but this effect was not uniform over the spectrum. The combined integrated line flux over the entire continuum normalized spectrum for the largest value of chemical heating efficiency (series chem5) increased by only a factor 0.046 over the baseline DIANA parameter value of 0.2. Some H₂O lines did increase in flux systematically (Figure 14).

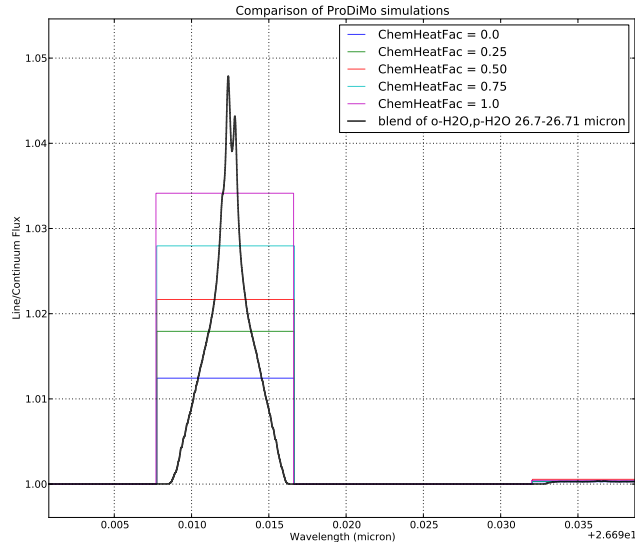
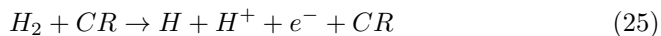
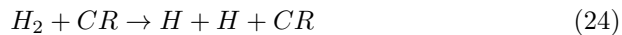
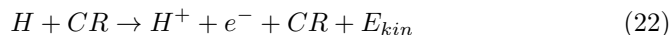


Figure 14: Increasing values of chemical heating efficiency may have boosted this H₂O line.

This line in Figure 14 is a blend of o- and p-H₂O at 26.7 and 26.71 μm and clearly it is boosted by the chemical heating, but not by a factor of 20.

3.1.4 ProDiMo H₂ cosmic ray ionization parameter exploration

PPDs can be heated by high energy protons and Fe nuclei (both cosmic rays) through the ionization of atomic and molecular hydrogen. H₂ is primarily ionized rather than dissociated. Cosmic ray particles lose only a small fraction of their kinetic energy in each collision, and will release 3.5 and 8eV of heat into the gas for H and H₂ ionization respectively.



[Kwok, 2007, Draine, 2011]

A series of ProDiMo simulations adjusting the cosmic ray ionization of H₂ on the FT Tau disk was performed. Altering this parameter should increase ionization throughout the disk but particularly influence the heating of the disk mid-plane which is shielded from virtually all stellar photons, while cosmic rays can penetrate deeply into the densest regions of the disk.

Simulation	ray1	ray2	ray3	ray4	ray5
CRI [1/s]	1.60x10 ⁻¹⁸	4.25x10 ⁻¹⁸	1.70x10 ⁻¹⁷	6.80x10 ⁻¹⁷	2.72x10 ⁻¹⁶

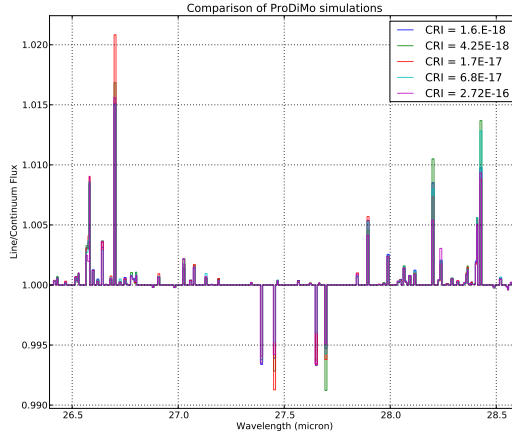


Figure 15: Detail of continuum normalized cosmic ray ionization efficiency series.

While some line fluxes were increased, the effect was sporadic and no clear relationship emerged relating total integrated line over continuum flux.

3.1.5 ProDiMo stellar parameter exploration

Stellar parameters for this series were generated for a range of stars aged 1Myr with metallicity $Z = 0.02$ and taken from the [Siess et al., 2000] isochrone calculator for pre-main sequence low mass stars with the exception of s1, a simulated brown dwarf whose parameters for ProDiMo were taken from [Muthusubramanian, 2014].

Disk masses for this series were based on the canonical $\rho_d/\rho = 0.01$ and not intended to replicate FT Tau but rather inform generically the effect of stellar parameter adjustment on line over continuum flux. Stellar parameters for FT Tau are well constrained and changing stellar parameters so dramatically will influence the SED [Garufi et al., 2016].

Simulation	s1	s2	s3	s4	s5	s6
Stellar Mass [M_\odot]	0.08	0.1	0.2	0.3	0.5	1
Luminosity [L_\odot]	0.025	0.0085	0.3045	0.6887	0.9288	2.335
Temperature [K]	2700	2928	3075	3360	3771	4278

While line over continuum flux was increased more significantly than by any other parameter adjustment (up to and beyond the factor of 20), changing stellar parameters leads to a loss of fit for the continuum and so the results are discarded.

3.2 The Spectral Atlas

Given that the parameter space exploration failed to acceptably resolve the factor ~ 20 line flux discrepancy estimated to exist between the *Spitzer* and

ProDiMo+FLiTs FT Tau spectra, the ProDiMo+FLiTs line fluxes are increased artificially relative to the continuum by the factor 20. The results have been binned to replicate the spectral resolution of the MIRI MRS and are included in the appendix.

3.3 Exposure Time Results

Several simple organic species are omitted from the exposure time calculations. The molecules C_2H_2 , C_2H , CH_4 , CH_3OH , CH^+ , CN , CS , H_2CO , HCO^+ , and HCS^+ are not considered because they either were not included in the ProDiMo chemistry set, do not have emission lines in the MIR, or did not produce sufficient line flux relative to the continuum for their detectability to be inferred from the sensitivity plots.

Table 5: Exposure Time Results

line [μm]	20s [Jy]	200s [Jy]	F_c [Jy]	F_l [Jy]
H ₂ O				
14.20	0.000620	0.000196	0.263346	0.017852
21.84	0.006637	0.002099	0.486774	0.032072
23.85	0.011044	0.003492	0.523444	0.068441
25.06	0.014649	0.004632	0.539161	0.098211
26.70	0.027313	0.008637	0.586709	0.142223
NH ₃				
10.61	0.000425	0.000134	0.330374	0.022089
HCN				
14.04	0.000654	0.000207	0.263346	0.035509

In Table 5, the '20s' and '200s' columns represent the limiting sensitivity for a 3σ detection of the features in the 'line' column for a 20 and 200 second exposure, respectively. The F column lists the ProDiMo computed flux (of the combined continuum+line flux) at the given wavelength. All lines in the sample are thus detectable at either exposure. A detailed quantitative exposure time calculator tool for this exact purpose is currently in development.

4 Discussion

4.1 Contrasting ProDiMo+FLiTs and Spitzer

The initial comparison of the model and data in section 3.1 based on the original DIANA parameters shows us that the gas emission line fluxes are significantly too low. How can this be a certain judgment? We begin with the *a priori* assumption that H₂O has been detected in FT Tau by *Spitzer* (with assumption detailed also in section 3.1). But what other evidence is there that H₂O exists in the FT Tau PPD? *Herschel* puts only an upper limit on o-H₂O emission at 63.32 μm of $< 1.25 * 10^{-17} W/m^2$, which would represent emission from a slightly larger radius and slightly greater scale height than the 15.74 μm H₂O

line emission [Riviere-Marichalar et al., 2012]. Another *Spitzer* observation reported the detection of HCN and H₂O from the FT Tau PPD at a signal-to-noise ratio (SNR) of 245 using the 17.12, 17.22 and 17.36 μ m H₂O lines [Najita et al., 2013].

However there still exist some potential issues with the approach of using the H₂O lines as reference. The H₂O lines in FLiTs were not uniformly influenced by the parameters that were adjusted; and a single line complex could not be representative of all the relative line flux levels between the ProDiMo+FLiTs results and *Spitzer*. Additionally, while some H₂O lines seem to be apparent in *Spitzer* data, several are conspicuously absent. Why would the 21.85 μ m line appear so prominently from *Spitzer* but not 21 or 25.36 μ m?

4.1.1 Continuum Flux ProDiMo+FLiTs vs. *Spitzer* FT Tau

As noted in section 3.1 the continuum flux model for *Spitzer* and ProDiMo+FLiTs is different in several wavelength ranges (also see Figure 7). One possibility is that there is a problem with the models. However, it must be noted that the *Spitzer* spectrum as presented in this thesis is a combination of two overlapping spectra generated from two different *Spitzer* IRS modules. The SH module covers 9.89-19.51 μ m and the LH module 18.83-37.14 μ m, where the spectral resolution is approximated as R=600 for both (it is not perfectly constant over these ranges). The sensitivity and SNR of the instrument is subject to rapid change near the boundaries of the wavelength range of these modules, hence the overlap regions differ significantly. To combine them the weighted mean of the spectra has been computed such that the closer a flux value is to the module wavelength range edge, the lesser the weight of the respective spectra's flux value. Additionally, as the *Spitzer* data is not a simulation, which flux constitutes the continuum must be modeled based on some assumptions regarding the presence of lines and noise.

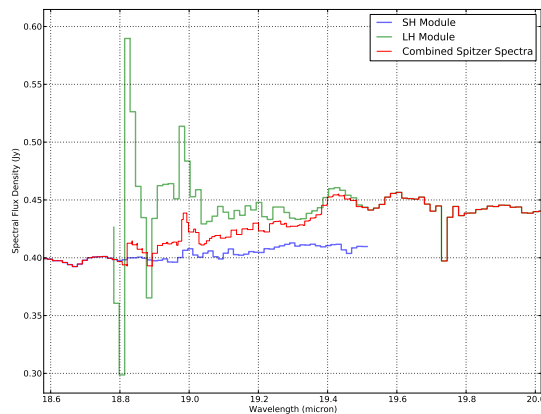


Figure 16: The combination of the two separate Spitzer spectra.

As a result, comparison of ProDiMo+FLiTs and *Spitzer* should be avoided in the interval 18.83-19.51 μ m.

4.2 M_{gas} and Impossible Disks

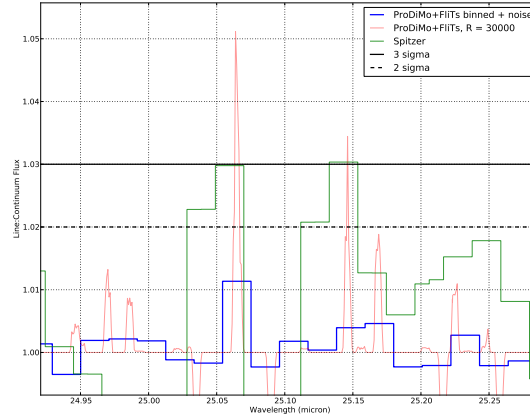


Figure 17: The massive $3.71M_{\odot}$ PPD simulation is unable to boost line flux sufficiently to match that of *Spitzer's* FT Tau spectrum.

The DIANA inferred gas mass of the FT Tau PPD may be too small. The series of M_{gas} tests demonstrate that gas emission can be increased but even when considering physically improbable disk masses the corresponding increase in line flux is insufficient. This relationship between increasing gas mass and line flux is represented in Figure 18. The relationship is linear at masses greater than the *a priori* gas mass so achieving a boost of the line flux by the required factor 20 has a corresponding disk mass approaching the mass of the most massive stars in existence. Interestingly [Meijerink et al., 2009] found that the gas-to-dust ratio may be one to two orders of magnitude higher than the canonical interstellar medium ratio of 0.01 when studying warm H_2O MIR emission from the inner disk of PPDs with *Spitzer*. The results in this thesis could be reconciled if one were to consider a varying dust to gas mass ratio in the disk which changes with radius, specifically for the inner region of the disk from which this H_2O emission originates, then the disk mass would not need to be increased as a whole to such large figures to match the observed line flux. This is worth further study.

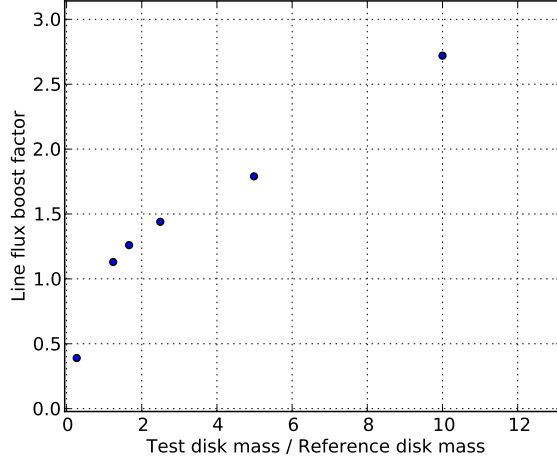


Figure 18: How changing the disk gas mass altered the total integrated line flux over the Spitzer-MIRI wavelength overlap range. A 'line flux boost factor' of 1 represents no change.

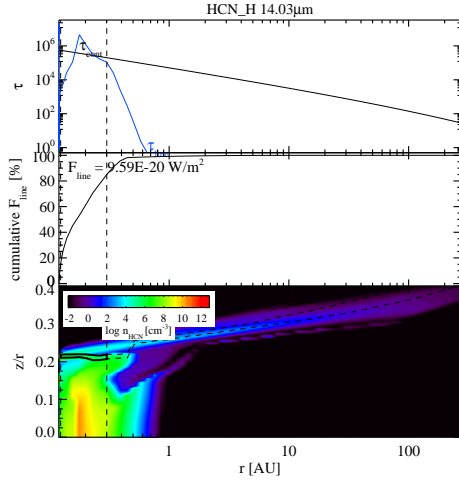
Consider the continuum flux changes in Figure 11. While dust is responsible for the continuum emission the dust mass was unchanged in the simulation series. This particular series of simulations was restarted from an old solution to the continuum radiative transfer of a previous simulation. In the continuum radiative transfer step of ProDiMo, information can only travel over one optical length during each iteration, and in the disk model with high optical depth ($> 10^6$) the new solution slowly drifts but does not eventually converge. Thus this is most likely an artifact of the simulation process.

In Figure 11 the $14.03\mu\text{m}$ HCN feature shifts from absorption to emission as the gas mass is increased. Upon inspection of the emitting region of the species a possible explanation presents itself in Figure 19.

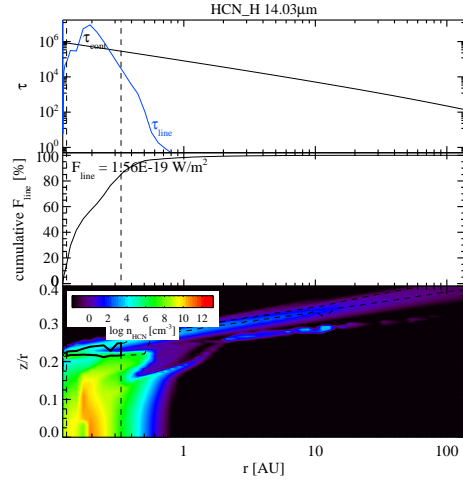
In the DIANA FT Tau simulation, the region from which the ro-vibrational HCN emission is generated appears to lie below a layer of cooler HCN gas. The heated surface of the disk directly exposed to the stellar radiation can be seen in Figure 20. The HCN emission region in the DIANA FT Tau simulation stretches radially outward to 0.2AU and is flattened vertically at $z/r \approx 0.22$. HCN is present in a layer that extends outwards to $R \approx 100\text{AU}$. Given the inclination of the disk and the flaring at large radii, this cold HCN layer may lie along the line of site to the emission region. In the dg6 simulation, the emitting region extends vertically further upwards, possibly to a more optically thin region from which the emission can escape.

4.3 Other ProDiMo Parameter Explorations

The other parameter space explorations resulted in no uniform and systematic improvement to the line over continuum flux ratio and hence their results are not used for further analysis. It is worth speculating why altering these other parameters did not influence gas emission flux in the desired way.

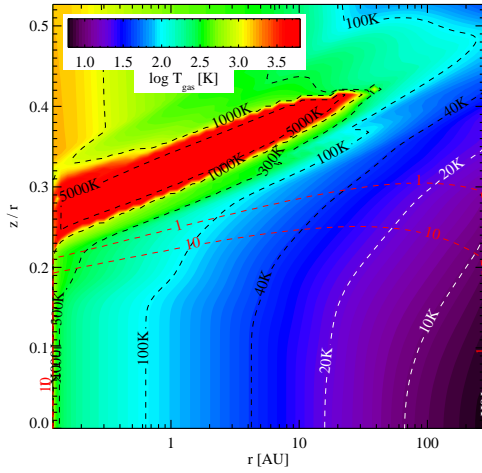


(a)DIANA FT Tau

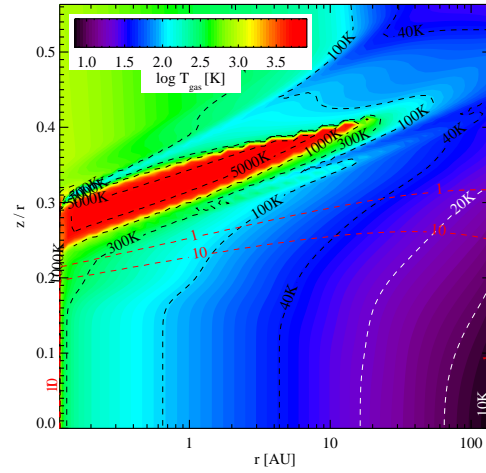


(b) dg6 FT Tau

Figure 19: Line analysis of 14.03μm Hydrogen Cyanide emission.



(a)DIANA FT Tau



(b) dg6 FT Tau

Figure 20: Gas temperature comparison.

The negative result from the cosmic ray ionization rate parameter tests could be explained by the cosmic ray heating influencing primarily the inner regions of the disk from which observed MIR emission does not originate. The PAH series also had a negative result. In order to heat the surrounding gas, PAHs require sufficient UV flux to be ionized and eject electrons into the the gas to begin heating. Classical T Tauri stars are less likely to exhibit PAH emission

relative to the more UV luminous Herbig AeBe stars [Kamp, 2011]. The UV flux of the FT Tau model may simply be insufficient to drive efficient PAH heating, regardless of the PAH abundance. The series which altered chemical heating efficiency produced the result that only some lines, namely H₂O lines at wavelengths greater than 20 μ m saw increases in flux. These results are difficult to explain without a deeper analysis.

5 Conclusion

The need for a detailed and quantitative exposure time calculator for the JWST MIRI MRS detector is clear. Without it, crude approximations must be made with overly simplifying assumptions. The relevance of the results to line over continuum emission and thus specific species detection is tenuous. Fortunately such a calculator is currently in development by the STScI.

There are discrepancies between the currently accepted model for FT Tau and the data from *Spitzer*. Namely, the line over continuum flux as computed by ProDiMo+FLiTs in the MIR is too low. Several attempts to reconcile this difference have been undertaken with mixed results. The most promising possibility remains a variable dust to gas ratio with radius. With such an adjustment to the model, potentially line emission in the inner disk region could be increased without needing to resort to a physically unlikely disk configuration.

References

- [Hol, 2005] (2005). Modern spectroscopy, 4th edition (j. michael hollas). *Journal of Chemical Education*, 82(1):43.
- [Aitken, 1906] Aitken, R. G. (1906). The Nebular Hypothesis. *Publications of the Astronomical Society of the Pacific*, 18:111.
- [ALMA Partnership et al., 2015] ALMA Partnership, Brogan, C. L., Pérez, L. M., Hunter, T. R., Dent, W. R. F., Hales, A. S., Hills, R. E., Corder, S., Fomalont, E. B., Vlahakis, C., Asaki, Y., Barkats, D., Hirota, A., Hodge, J. A., Impellizzeri, C. M. V., Kneissl, R., Liuzzo, E., Lucas, R., Marcelino, N., Matsushita, S., Nakanishi, K., Phillips, N., Richards, A. M. S., Toledo, I., Aladro, R., Brogiere, D., Cortes, J. R., Cortes, P. C., Espada, D., Galarza, F., Garcia-Appadoo, D., Guzman-Ramirez, L., Humphreys, E. M., Jung, T., Kamenno, S., Laing, R. A., Leon, S., Marconi, G., Mignano, A., Nikolic, B., Nyman, L.-A., Radiszcz, M., Remijan, A., Rodón, J. A., Sawada, T., Takahashi, S., Tilanus, R. P. J., Vila Vilaro, B., Watson, L. C., Wiklind, T., Akiyama, E., Chapillon, E., de Gregorio-Monsalvo, I., Di Francesco, J., Gueth, F., Kawamura, A., Lee, C.-F., Nguyen Luong, Q., Mangum, J., Pietu, V., Sanhueza, P., Saigo, K., Takakuwa, S., Ubach, C., van Kempen, T., Wootten, A., Castro-Carrizo, A., Francke, H., Gallardo, J., Garcia, J., Gonzalez, S., Hill, T., Kaminski, T., Kurono, Y., Liu, H.-Y., Lopez, C., Morales, F., Plarre, K., Schieven, G., Testi, L., Videla, L., Villard, E., Andreani, P., Hibbard, J. E., and Tatematsu, K. (2015). The 2014 ALMA Long Baseline Campaign: First Results from High Angular Resolution Observations toward the HL Tau Region. *The Astrophysical Journal Letters*, 808:L3.
- [Andrews et al., 2013] Andrews, S. M., Rosenfeld, K. A., Kraus, A. L., and Wilner, D. J. (2013). The Mass Dependence between Protoplanetary Disks and their Stellar Hosts. *The Astrophysical Journal*, 771:129.
- [Andrews et al., 2009] Andrews, S. M., Wilner, D. J., Hughes, A. M., Qi, C., and Dullemond, C. P. (2009). Protoplanetary Disk Structures in Ophiuchus. *The Astrophysical Journal*, 700:1502–1523.
- [Andrews et al., 2010] Andrews, S. M., Wilner, D. J., Hughes, A. M., Qi, C., and Dullemond, C. P. (2010). Protoplanetary Disk Structures in Ophiuchus. II. Extension to Fainter Sources. *The Astrophysical Journal*, 723:1241–1254.
- [Anthonioz et al., 2015] Anthonioz, F., Ménard, F., Pinte, C., Le Bouquin, J.-B., Benisty, M., Thi, W.-F., Absil, O., Duchêne, G., Augereau, J.-C., Berger, J.-P., Casassus, S., Duvert, G., Lazareff, B., Malbet, F., Millan-Gabet, R., Schreiber, M. R., Traub, W., and Zins, G. (2015). The VLTI/PIONIER near-infrared interferometric survey of southern T Tauri stars. I. First results. *Astronomy and Astrophysics*, 574:A41.
- [Antonellini et al., 2016] Antonellini, S., Kamp, I., Lahuis, F., Woitke, P., Thi, W.-F., Meijerink, R., Aresu, G., Spaans, M., Güdel, M., and Liebhart, A. (2016). Mid-IR spectra of pre-main sequence Herbig stars: An explanation for the non-detections of water lines. *Astronomy and Astrophysics*, 585:A61.

- [Artymowicz and Lubow, 1994] Artymowicz, P. and Lubow, S. H. (1994). Dynamics of binary-disk interaction. 1: Resonances and disk gap sizes. *The Astrophysical Journal*, 421:651–667.
- [Aumann et al., 1984] Aumann, H. H., Beichman, C. A., Gillett, F. C., de Jong, T., Houck, J. R., Low, F. J., Neugebauer, G., Walker, R. G., and Wesselius, P. R. (1984). Discovery of a shell around Alpha Lyrae. *The Astrophysical Journal*, 278:L23–L27.
- [Barnes, 2001] Barnes, J. (2001). *Early Greek Philosophy*. Classics Series. Penguin.
- [Bast et al., 2013] Bast, J. E., Lahuis, F., van Dishoeck, E. F., and Tielens, A. G. G. M. (2013). Exploring organic chemistry in planet-forming zones. *Astronomy and Astrophysics*, 551:A118.
- [Beckwith et al., 1986] Beckwith, S., Sargent, A. I., Scoville, N. Z., Masson, C. R., Zuckerman, B., and Phillips, T. G. (1986). Small-scale structure of the circumstellar gas of HL Tauri and R Monocerotis. *The Astrophysical Journal*, 309:755–761.
- [Bertout, 1989] Bertout, C. (1989). T Tauri stars - Wild as dust. *Annual review of astronomy and astrophysics*, 27:351–395.
- [Bouvier and Wadhwa, 2010] Bouvier, A. and Wadhwa, M. (2010). The age of the Solar System redefined by the oldest Pb-Pb age of a meteoritic inclusion. *Nature Geoscience*, 3:637–641.
- [Burrows et al., 1996] Burrows, C. J., Stapelfeldt, K. R., Watson, A. M., Krist, J. E., Ballester, G. E., Clarke, J. T., Crisp, D., Gallagher, III, J. S., Griffiths, R. E., Hester, J. J., Hoessel, J. G., Holtzman, J. A., Mould, J. R., Scowen, P. A., Trauger, J. T., and Westphal, J. A. (1996). Hubble Space Telescope Observations of the Disk and Jet of HH 30. *The Astrophysical Journal*, 473:437.
- [Carr and Najita, 2008] Carr, J. and Najita, J. R. (2008). Organic molecules and water in the planet formation region of young circumstellar disks. *Science*, 319(5869):1504–1506.
- [Carr and Najita, 2011] Carr, J. S. and Najita, J. R. (2011). Organic Molecules and Water in the Inner Disks of T Tauri Stars. *The Astrophysics Journal*, 733:102.
- [Crutcher et al., 2009] Crutcher, R. M., Hakobian, N., and Troland, T. H. (2009). Testing Magnetic Star Formation Theory. *Astrophysical Journal*, 692:844–855.
- [Draine, 2011] Draine, B. T. (2011). *Physics of the Interstellar and Intergalactic Medium*.
- [Evans, 1993] Evans, A. (1993). *The Dusty Universe*. Ellis Horwood library of space science and space technology: Series in astronomy. Ellis Horwood.

- [Garufi et al., 2016] Garufi, A., Quanz, S. P., Schmid, H. M., Mulders, G. D., Avenhaus, H., Boccaletti, A., Ginski, C., Langlois, M., Stolker, T., Augereau, J.-C., Benisty, M., Lopez, B., Dominik, C., Gratton, R., Henning, T., Janson, M., Ménard, F., Meyer, M. R., Pinte, C., Sissa, E., Vigan, A., Zurlo, A., Bazzon, A., Buenzli, E., Bonnefoy, M., Brandner, W., Chauvin, G., Cheetham, A., Cudel, M., Desidera, S., Feldt, M., Galicher, R., Kasper, M., Lagrange, A.-M., Lannier, J., Maire, A. L., Mesa, D., Mouillet, D., Peretti, S., Perrot, C., Salter, G., and Wildi, F. (2016). The SPHERE view of the planet-forming disk around HD 100546. *Astronomy and Astrophysics*, 588:A8.
- [Girart et al., 2006] Girart, J. M., Rao, R., and Marrone, D. P. (2006). Magnetic Fields in the Formation of Sun-Like Stars. *Science*, 313:812–814.
- [Glasse et al., 2015] Glasse, A., Rieke, G. H., Bauwens, E., García-Marín, M., Ressler, M. E., Rost, S., Tikkanen, T. V., Vandenbussche, B., and Wright, G. S. (2015). The Mid-Infrared Instrument for the James Webb Space Telescope, IX: Predicted Sensitivity. *Publications of the Astronomical Society of Pacific*, 127:686–695.
- [Gray, 2007] Gray, R. O. (2007). The Problems with Vega. In Sterken, C., editor, *The Future of Photometric, Spectrophotometric and Polarimetric Standardization*, volume 364 of *Astronomical Society of the Pacific Conference Series*, page 305.
- [Greaves, 2004] Greaves, J. S. (2004). Dense gas discs around T Tauri stars. *Monthly Notices of the Royal Astronomical Society*, 351:L99–L104.
- [Güdel et al., 2007] Güdel, M., Briggs, K. R., Arzner, K., Audard, M., Bouvier, J., Feigelson, E. D., Franciosini, E., Glauser, A., Grosso, N., Micela, G., Monin, J.-L., Montmerle, T., Padgett, D. L., Palla, F., Pillitteri, I., Rebull, L., Scelsi, L., Silva, B., Skinner, S. L., Stelzer, B., and Telleschi, A. (2007). The XMM-Newton extended survey of the Taurus molecular cloud (XEST). *Astronomy and Astrophysics*, 468:353–377.
- [Guilloteau et al., 2016] Guilloteau, S., Piétu, V., Chapillon, E., Di Folco, E., Dutrey, A., Henning, T., Semenov, D., Birnstiel, T., and Grosso, N. (2016). The shadow of the Flying Saucer: A very low temperature for large dust grains. *Astronomy and Astrophysics*, 586:L1.
- [Hartmann et al., 1998] Hartmann, L., Calvet, N., Gullbring, E., and D’Alessio, P. (1998). Accretion and the Evolution of T Tauri Disks. *The Astrophysical Journal*, 495:385–400.
- [Helou and Walker, 1988] Helou, G. and Walker, D. W., editors (1988). *Infrared astronomical satellite (IRAS) catalogs and atlases. Volume 7: The small scale structure catalog*, volume 7.
- [Hoyle, 1960] Hoyle, F. (1960). The Origin of the Solar Nebula. *Quarterly Journal of the Royal Astronomical Society*, 1:28.
- [Isella et al., 2009] Isella, A., Carpenter, J. M., and Sargent, A. I. (2009). Structure and evolution of pre-main-sequence circumstellar disks. *The Astrophysical Journal*, 701(1):260.

- [Jeans, 1902] Jeans, J. H. (1902). The Stability of a Spherical Nebula. *Philosophical Transactions of the Royal Society of London Series A*, 199:1–53.
- [Jørgensen et al., 2005] Jørgensen, J. K., Bourke, T. L., Myers, P. C., Schöier, F. L., van Dishoeck, E. F., and Wilner, D. J. (2005). Probing the Inner 200 AU of Low-Mass Protostars with the Submillimeter Array: Dust and Organic Molecules in NGC 1333 IRAS 2A. *The Astrophysical Journal*, 632:973–981.
- [Kamp, 2011] Kamp, I. (2011). Evolution of PAHs in Protoplanetary Disks. In Joblin, C. and Tielens, A. G. G. M., editors, *EAS Publications Series*, volume 46 of *EAS Publications Series*, pages 271–283.
- [Kamp and Bertoldi, 2000] Kamp, I. and Bertoldi, F. (2000). CO in the circumstellar disks of Vega and beta Pictoris. *Astronomy and Astrophysics*, 353:276–286.
- [Kenyon et al., 2008] Kenyon, S. J., Gómez, M., and Whitney, B. A. (2008). *Low Mass Star Formation in the Taurus-Auriga Clouds*, page 405.
- [Kenyon and Hartmann, 1987] Kenyon, S. J. and Hartmann, L. (1987). Spectral energy distributions of T Tauri stars - Disk flaring and limits on accretion. *The Astrophysical Journal*, 323:714–733.
- [Kopparapu et al., 2013] Kopparapu, R. K., Ramirez, R., Kasting, J. F., Eymet, V., Robinson, T. D., Mahadevan, S., Terrien, R. C., Domagal-Goldman, S., Meadows, V., and Deshpande, R. (2013). Habitable Zones around Main-sequence Stars: New Estimates. *The Astrophysical Journal*, 765:131.
- [Kuhi, 1966] Kuhi, L. V. (1966). T Tauri Stars: A Short Review. *Journal of the Royal Astronomical Society of Canada*, 60:1.
- [Kwok, 2007] Kwok, S. (2007). *Physics and Chemistry of the Interstellar Medium*. University Science Books.
- [Lahuis et al., 2006] Lahuis, F., van Dishoeck, E. F., Boogert, A. C. A., Pontoppidan, K. M., Blake, G. A., Dullemond, C. P., Evans, II, N. J., Hogerheijde, M. R., Jørgensen, J. K., Kessler-Silacci, J. E., and Knez, C. (2006). Hot Organic Molecules toward a Young Low-Mass Star: A Look at Inner Disk Chemistry. *Astronomy and Astrophysics*, 636:L145–L148.
- [LeBlanc, 2010] LeBlanc, F. (2010). *An Introduction to Stellar Astrophysics*.
- [Lecar et al., 2006] Lecar, M., Podolak, M., Sasselov, D., and Chiang, E. (2006). On the Location of the Snow Line in a Protoplanetary Disk. *The Astrophysical Journal*, 640:1115–1118.
- [Lee et al., 2008] Lee, J.-E., Bergin, E. A., and Lyons, J. R. (2008). Oxygen isotope anomalies of the Sun and the original environment of the solar system. *Meteoritics and Planetary Science*, 43:1351–1362.
- [Luhman et al., 2009] Luhman, K. L., Mamajek, E. E., Allen, P. R., Muench, A. A., and Finkbeiner, D. P. (2009). Discovery of a Wide Binary Brown Dwarf Born in Isolation. *The Astrophysical Journal*, 691:1265–1275.

- [Lynden-Bell and Pringle, 1974] Lynden-Bell, D. and Pringle, J. E. (1974). The evolution of viscous discs and the origin of the nebular variables. *Monthly Notices of the Royal Astronomical Society*, 168:603–637.
- [Mamajek, 2005] Mamajek, E. E. (2005). A Moving Cluster Distance to the Exoplanet 2M1207b in the TW Hydrae Association. *The Astrophysical Journal*, 634:1385–1394.
- [Mamajek, 2009] Mamajek, E. E. (2009). Initial Conditions of Planet Formation: Lifetimes of Primordial Disks. In Usuda, T., Tamura, M., and Ishii, M., editors, *American Institute of Physics Conference Series*, volume 1158 of *American Institute of Physics Conference Series*, pages 3–10.
- [McElroy et al., 2013] McElroy, D., Walsh, C., Markwick, A. J., Cordiner, M. A., Smith, K., and Millar, T. J. (2013). The UMIST database for astrochemistry 2012. *Astronomy and Astrophysics*, 550:A36.
- [McKee and Ostriker, 2007] McKee, C. F. and Ostriker, E. C. (2007). Theory of Star Formation. *Annual Review of Astronomy and Astrophysics*, 45:565–687.
- [Meijerink et al., 2009] Meijerink, R., Pontoppidan, K. M., Blake, G. A., Poelman, D. R., and Dullemond, C. P. (2009). Radiative Transfer Models of Mid-Infrared H₂O Lines in the Planet-Forming Region of Circumstellar Disks. *The Astrophysical Journal*, 704:1471–1481.
- [Miotello et al., 2016] Miotello, A., van Dishoeck, E. F., Kama, M., and Bruderer, S. (2016). Determining protoplanetary disk gas masses from CO isotopologues line observations. *ArXiv e-prints*.
- [Montgomery et al., 2009] Montgomery, C., Orchiston, W., and Whittingham, I. (2009). Michell, Laplace and the origin of the black hole concept. *Journal of Astronomical History and Heritage*, 12:90–96.
- [Morton et al., 2016] Morton, T. D., Bryson, S. T., Coughlin, J. L., Rowe, J. F., Ravichandran, G., Petigura, E. A., Haas, M. R., and Batalha, N. M. (2016). False Positive Probabilities for all Kepler Objects of Interest: 1284 Newly Validated Planets and 428 Likely False Positives. *The Astrophysical Journal*, 822:86.
- [Muthusubramanian, 2014] Muthusubramanian, B. (2014). Structural and chemical comparison of brown dwarf protoplanetary disks with t tauri and herbig disks. Master’s thesis, Rijksuniversiteit Groningen, the Netherlands.
- [Najita et al., 2013] Najita, J. R., Carr, J. S., Pontoppidan, K. M., Salyk, C., van Dishoeck, E. F., and Blake, G. A. (2013). The HCN-Water Ratio in the Planet Formation Region of Disks. *The Astrophysical Journal*, 766:134.
- [O’dell et al., 1993] O’dell, C. R., Wen, Z., and Hu, X. (1993). Discovery of new objects in the Orion nebula on HST images - Shocks, compact sources, and protoplanetary disks. *The Astrophysical Journal*, 410:696–700.
- [Petigura et al., 2013] Petigura, E. A., Howard, A. W., and Marcy, G. W. (2013). Prevalence of Earth-size planets orbiting Sun-like stars. *Proceedings of the National Academy of Science*, 110:19273–19278.

- [Prentice, 1978] Prentice, A. J. R. (1978). Origin of the solar system. I - Gravitational contraction of the turbulent protosun and the shedding of a concentric system of gaseous Laplacian rings. *Moon and Planets*, 19:341–398.
- [Ressler et al., 2015] Ressler, M. E., Sukhatme, K. G., Franklin, B. R., Mahoney, J. C., Thelen, M. P., Bouchet, P., Colbert, J. W., Cracraft, M., Dicken, D., Gastaud, R., Goodson, G. B., Eccleston, P., Moreau, V., Rieke, G. H., and Schneider, A. (2015). The Mid-Infrared Instrument for the James Webb Space Telescope, VIII: The MIRI Focal Plane System. *Publications of the Astronomical Society of Pacific*, 127:675–685.
- [Ricci et al., 2008] Ricci, L., Robberto, M., and Soderblom, D. R. (2008). The Hubble Space Telescope/Advanced Camera for Surveys Atlas of Protoplanetary Disks in the Great Orion Nebula. *The Astrophysical Journal*, 136:2136–2151.
- [Rieke et al., 2015] Rieke, G. H., Wright, G. S., Böker, T., Bouwman, J., Colina, L., Glasse, A., Gordon, K. D., Greene, T. P., Güdel, M., Henning, T., Justtanont, K., Lagage, P.-O., Meixner, M. E., Nørgaard-Nielsen, H.-U., Ray, T. P., Ressler, M. E., van Dishoeck, E. F., and Waelkens, C. (2015). The Mid-Infrared Instrument for the James Webb Space Telescope, I: Introduction. *Publications of the Astronomical Society of Pacific*, 127:584–594.
- [Riviere-Marichalar et al., 2012] Riviere-Marichalar, P., Ménard, F., Thi, W. F., Kamp, I., Montesinos, B., Meeus, G., Woitke, P., Howard, C., Sandell, G., Podio, L., Dent, W. R. F., Mendigutía, I., Pinte, C., White, G. J., and Barrado, D. (2012). Detection of warm water vapour in Taurus protoplanetary discs by Herschel. *Astronomy and Astrophysics*, 538:L3.
- [Safronov, 1972] Safronov, V. S. (1972). *Evolution of the protoplanetary cloud and formation of the earth and planets*.
- [Sagan, 1979] Sagan, C. (1979). *Broca's brain: reflections on the romance of science*. Random House.
- [Scilla, 2016] Scilla, D. (2016). Introduction to stellar evolution. *Journal of Physics: Conference Series*, 703(1):012002.
- [Sephton, 2002] Sephton, M. A. (2002). Organic compounds in carbonaceous meteorites. *Nat. Prod. Rep.*, 19:292–311.
- [Siess et al., 2000] Siess, L., Dufour, E., and Forestini, M. (2000). An internet server for pre-main sequence tracks of low- and intermediate-mass stars. *Astronomy and Astrophysics*, 358:593–599.
- [Snytnikov et al., 2014] Snytnikov, V., Stoyanovskaya, O., and Rudina, N. (2014). Synthesis of Organic Matter of Prebiotic Chemistry at the Protoplanetary Disc. In *40th COSPAR Scientific Assembly*, volume 40 of *COSPAR Meeting*.
- [Thi et al., 2004] Thi, W.-F., van Zadelhoff, G.-J., and van Dishoeck, E. F. (2004). Organic molecules in protoplanetary disks around T Tauri and Herbig Ae stars. *Astronomy and Astrophysics*, 425:955–972.

- [van der Plas et al., 2015] van der Plas, G., van den Ancker, M. E., Waters, L. B. F. M., and Dominik, C. (2015). The structure of disks around Herbig Ae/Be stars as traced by CO ro-vibrational emission. *Astronomy and Astrophysics*, 574:A75.
- [van Zadelhoff et al., 2001] van Zadelhoff, G.-J., van Dishoeck, E. F., Thi, W.-F., and Blake, G. A. (2001). Submillimeter lines from circumstellar disks around pre-main sequence stars. *Astronomy and Astrophysics*, 377:566–580.
- [Vicente, S. M. and Alves, J., 2005] Vicente, S. M. and Alves, J. (2005). Size distribution of circumstellar disks in the trapezium cluster. *Astronomy and Astrophysics*, 441(1):195–205.
- [Walker, 2000] Walker, H. J. (2000). A brief history of infrared astronomy. *Astronomy and Geophysics*, 41(5):10.
- [Weiss and Marcy, 2014] Weiss, L. M. and Marcy, G. W. (2014). The Mass-Radius Relation for 65 Exoplanets Smaller than 4 Earth Radii. *The Astrophysical Journal Letters*, 783:L6.
- [Wells et al., 2015] Wells, M., Pel, J.-W., Glasse, A., Wright, G. S., Aitink-Kroes, G., Azzollini, R., Beard, S., Brandl, B. R., Gallie, A., Geers, V. C., Glauser, A. M., Hastings, P., Henning, T., Jager, R., Justtanont, K., Kruizinga, B., Lahuis, F., Lee, D., Martínez-Delgado, I., Martínez-Galarza, J. R., Meijers, M., Morrison, J. E., Müller, F., Nakos, T., O’Sullivan, B., Oudenhuisen, A., Parr-Burman, P., Pauwels, E., Rohloff, R.-R., Schmalzl, E., Sykes, J., Thelen, M. P., van Dishoeck, E. F., Vandenbussche, B., Venema, L. B., Visser, H., Waters, L. B. F. M., and Wright, D. (2015). The Mid-Infrared Instrument for the James Webb Space Telescope, VI: The Medium Resolution Spectrometer. *Publications of the Astronomical Society of Pacific*, 127:646–664.
- [Whitrow, 1967] Whitrow, G. J. (1967). Kant and the Extragalactic Nebulae. *Quarterly Journal of the Royal Astronomical Society*, 8:48.
- [Williams and Cecchi-Pestellini, 2016] Williams, D. A. and Cecchi-Pestellini, C. (2016). *The Chemistry of Cosmic Dust*. The Royal Society of Chemistry.
- [Williams and Cieza, 2011] Williams, J. P. and Cieza, L. A. (2011). Protoplanetary Disks and Their Evolution. *Annual Review of Astronomy and Astrophysics*, 49:67–117.
- [Woitke et al., 2009] Woitke, P., Kamp, I., and Thi, W.-F. (2009). Radiation thermo-chemical models of protoplanetary disks. I. Hydrostatic disk structure and inner rim. *The Astrophysical Journal*, 501:383–406.
- [Woitke et al., 2016] Woitke, P., Min, M., Pinte, C., Thi, W.-F., Kamp, I., Rab, C., Anthonioz, F., Antonellini, S., Baldovin-Saavedra, C., Carmona, A., Dominik, C., Dionatos, O., Greaves, J., Güdel, M., Ilee, J. D., Liebhart, A., Ménard, F., Rigon, L., Waters, L. B. F. M., Aresu, G., Meijerink, R., and Spaans, M. (2016). Consistent dust and gas models for protoplanetary disks. I. Disk shape, dust settling, opacities, and PAHs. *Astronomy and Astrophysics*, 586:A103.

[Woolfson, 1993] Woolfson, M. M. (1993). The Solar - Origin and Evolution. *Quarterly Journal of the Royal Astronomical Society*, 34.

[Zubko et al., 2004] Zubko, V., Dwek, E., and Arendt, R. G. (2004). Interstellar Dust Models Consistent with Extinction, Emission, and Abundance Constraints. *The Astrophysical Journal Supplement Series*, 152:211–249.

Appendices

Appendix I, The Spectral Atlas

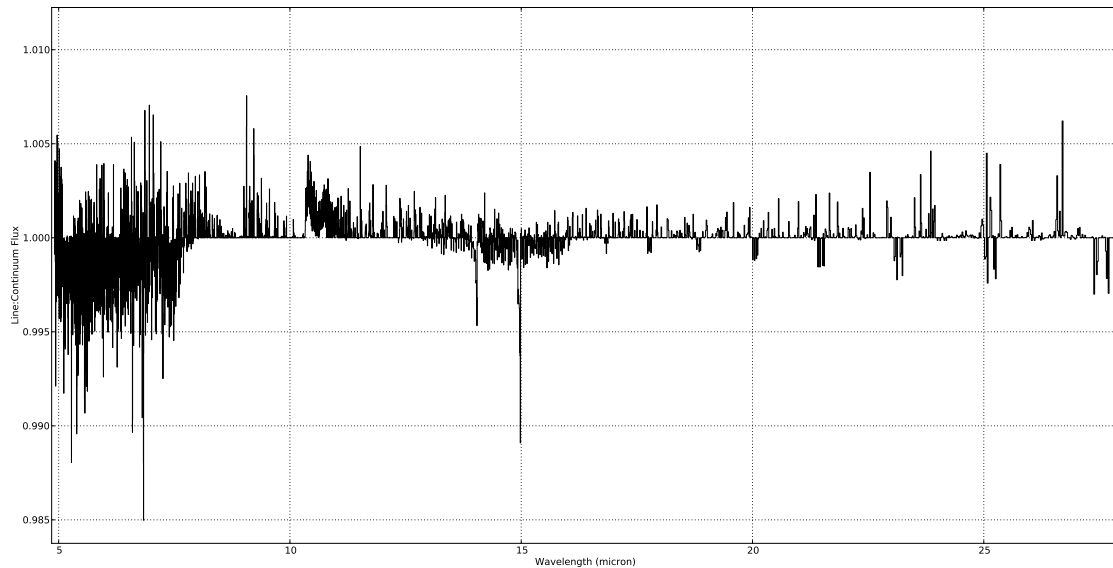


Figure 21: The ProDiMo+FLiTS DIANA standard FT Tau continuum normalized spectrum over the entire MIRI wavelength range and with corresponding MIRI spectral resolution approximated.

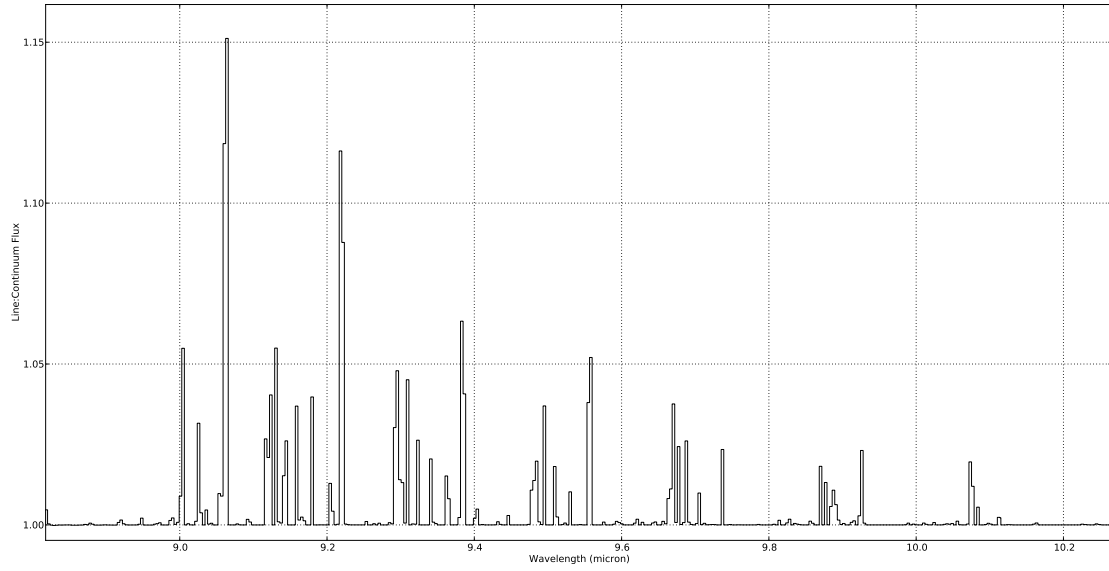


Figure 22: The continuum normalized ProDiMo+FLiTS DIANA standard FT Tau OH spectrum with line flux increased by a factor 20.

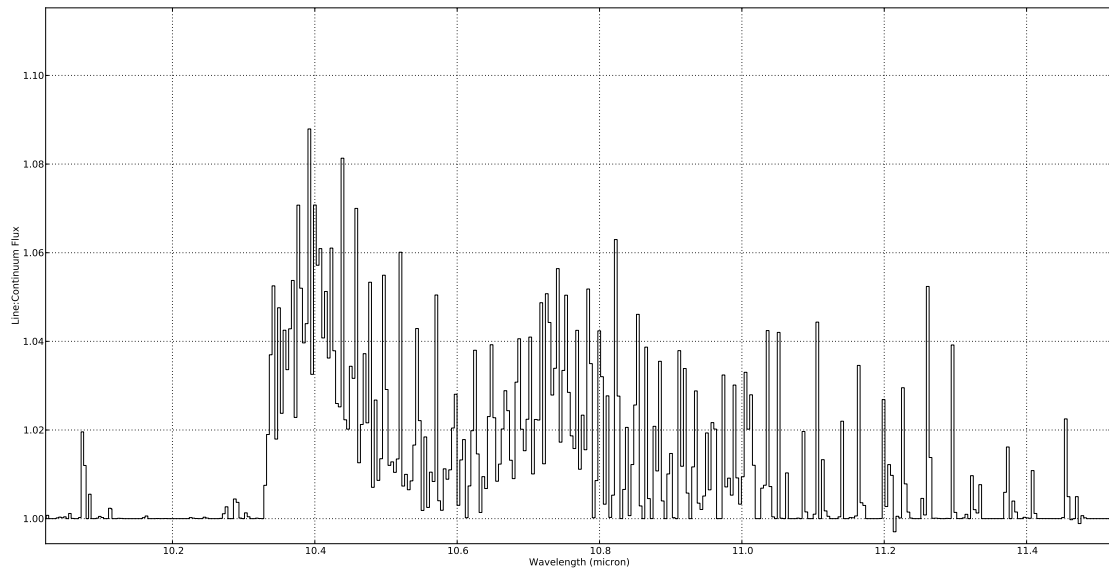


Figure 23: The continuum normalized ProDiMo+FLiTS DIANA standard FT Tau NH3 spectrum with line flux increased by a factor 20.

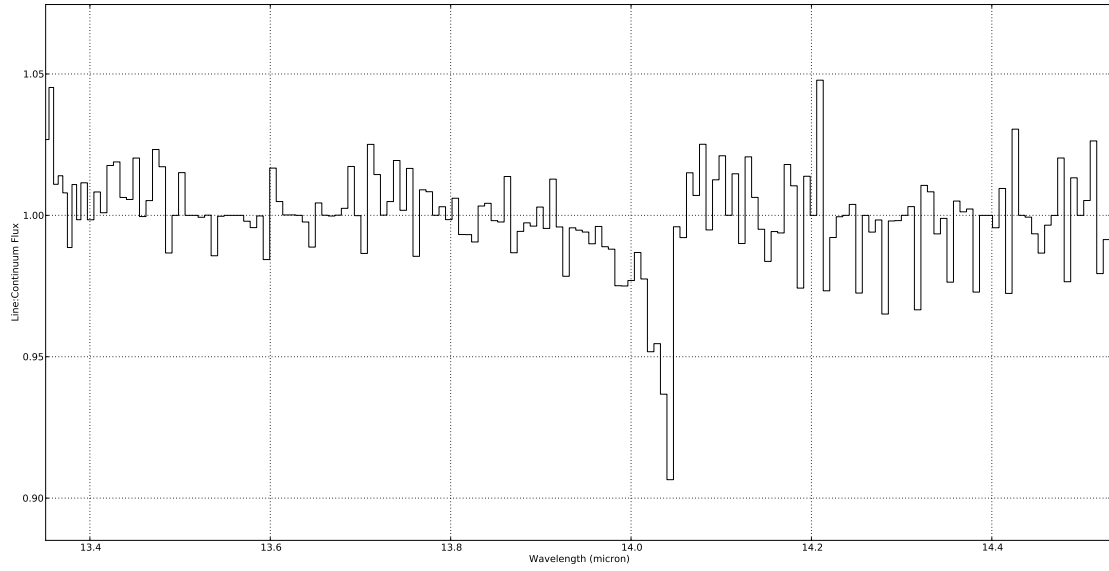


Figure 24: The continuum normalized ProDiMo+FLiTS DIANA standard FT Tau HNC spectrum with line flux increased by a factor 20.

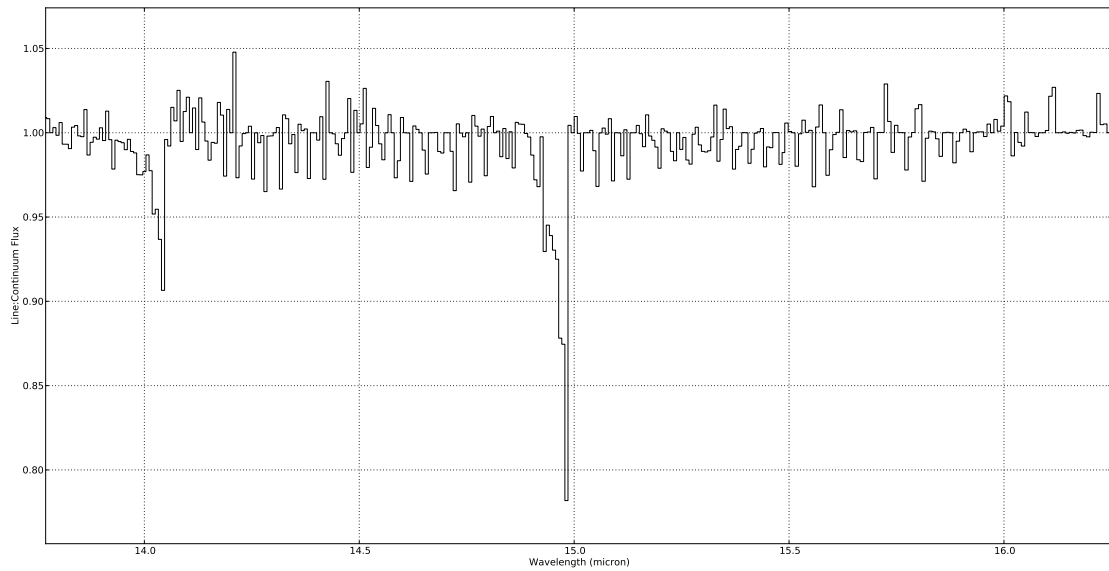


Figure 25: The continuum normalized ProDiMo+FLiTS DIANA standard FT Tau CO2 spectrum with line flux increased by a factor 20.

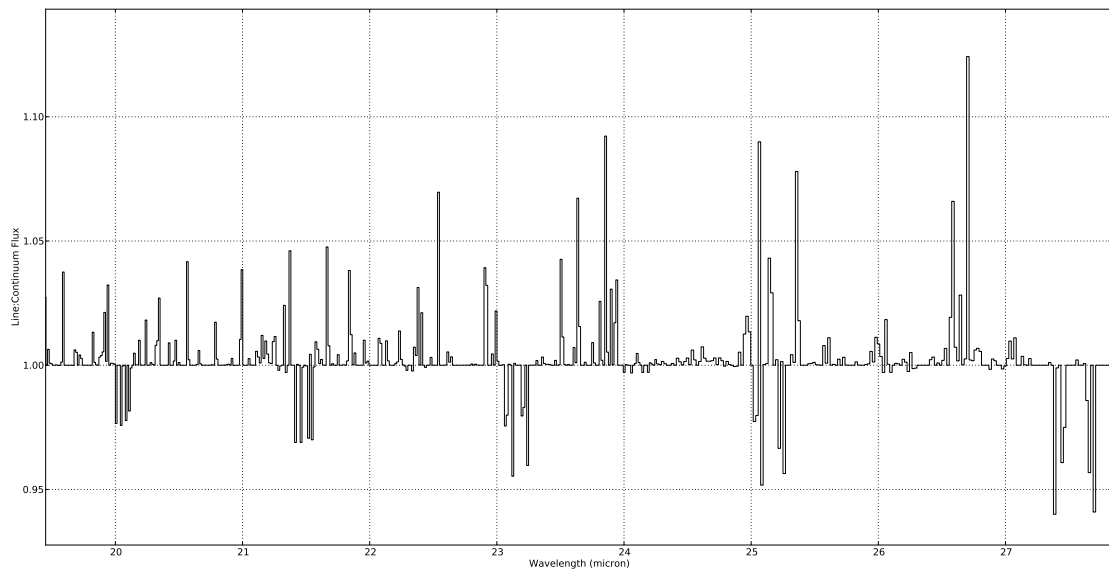


Figure 26: The continuum normalized ProDiMo+FLiTS DIANA standard FT Tau H₂O spectrum with line flux increased by a factor 20.